Theoretical investigation on spectroscopic properties of 18 Λ-S and 35 Ω states of SH^+ ion*

XING Wei[1,*], LI Shengzhou[1], ZHANG Fang[1], SUN Jinfeng[2], LI Wentao[3], ZHU Zunlüe[2]

1. College of Physics and Electronic Engineering, Xinyang Normal University, Xinyang 464000, China
2. School of Physics, Henan Normal University, Xinxiang 453000, China
3. Weifang University of Science and Technology, Shouguang 262700, China

Abstract

On the basis of precisely treating various physical effects—including core-valence electron correlation, scalar relativistic corrections, spin-orbit coupling, and extrapolation to the complete basis set limit, this study constructed the potential energy curves of 18 Λ-S states and the corresponding 35 Ω states of the SH^+ ion by means of the optimized icMRCI+*Q* method. Within the all-electron icMRCI/cc-pCV5Z+SOC theoretical framework, the transition dipole moment curves of 12 pairs of transitions between 7 Ω states[including $X^3\Sigma^-_{0^+}$, $X^3\Sigma^-_1$, $(1)2^{1\text{st well}}(\upsilon' = 0–8)$, $(2)0^+(\upsilon' = 0–5)$, $(2)2^{1\text{st well}}(\upsilon' = 0–2)$, $(2)1^{1\text{st well}}(\upsilon' = 0–2)$, and $(3)0^+(\upsilon' = 0–2)$] were calculated. Based on the aforementioned potential energy curves and transition dipole moment curves, the spectral data of each state and the transition data between Ω states were determined by solving the Schrödinger equation for nuclear motion and combining with the corresponding formulas, and the obtained results were in excellent agreement with the experimental values. In addition, the spectral characteristics of the 12 pairs of radiative transitions were clarified, the variation trends of the radiative lifetimes($\tau_{\upsilon'J'}$) and radiation widths(Γ_r) of the excited Ω states were revealed, and the influence of the rotational quantum number(J') on the radiative lifetimes($\tau_{\upsilon'J'}$) of the $(2)2^{1\text{st well}}(\upsilon' = 0–2, +)$, $(2)1^{1\text{st well}}(\upsilon' = 0–2, +)$, and $(3)0^+(\upsilon' = 0–2, +)$ states was discussed. The datasets presented in this paper, including the potential energy curves of 18 Λ-S and 35 Ω states, 12 pairs of transition dipole moments between the 7 Ω states[$X^3\Sigma^-_{0^+}$, $X^3\Sigma^-_1$, $(1)2^{1\text{st well}}(\upsilon' = 0–8)$, $(2)0^+(\upsilon' = 0–5)$, $(2)2^{1\text{st well}}(\upsilon' = 0–2)$, $(2)1^{1\text{st well}}(\upsilon' = 0–2)$, and $(3)0^+(\upsilon' = 0–2)$], and variations of the radiative lifetimes($\tau_{\upsilon'J'}$) with J' for the $(2)2^{1\text{st well}}(\upsilon' = 0–2, +)$, $(2)1^{1\text{st well}}(\upsilon' = 0–2, +)$, and $(3)0^+(\upsilon' = 0–2, +)$ states of

---

* The paper is an English translated version of the original Chinese paper published in Acta Physica Sinica. Please cite the paper as: XING Wei, LI Shengzhou, ZHANG Fang, SUN Jinfeng, LI Wentao, ZHU Zunlüe, **Theoretical investigation on spectroscopic properties of 18 Λ-S and 35 Ω states of SH^+ ion.** *Acta Phys. Sin.*, 2026, 75(5): 050305. DOI: 10.7498/aps.75.20251481

SH^+ ion, are openly available at
https://www.doi.org/10.57760/sciencedb.j00213.00233.

Keywords: scalar relativistic, spin-orbit coupling, potential energy curves, transition dipole moments, spectral data

doi: 10.7498/aps.75.20251481
cstr: 32037.14.aps.75.20251481

1 Introduction

SH^+ is a crucial ion in astrophysics and interstellar chemistry[1]. Since 2010, astronomers have detected SH^+ in various interstellar environments using advanced astronomical facilities[2-6]. For instance, Benz et al.[2], Godard et al.[3], and Möller et al.[4] employed the Heterodyne Instrument for the Far Infrared (HIFI) aboard the Herschel Space Observatory. They conducted spectral line surveys of the massive star-forming region W3 IRS5[2], diffuse interstellar clouds[3], and the molecular cloud Sagittarius B2(M) near the Galactic Center[4], respectively, and detected submillimeter-wave spectral lines of SH^+. Additionally, Müller et al.[5] and Muller et al.[6] detected SH^+ in the Orion Bar structure[5] and in a high-redshift absorber (the interstellar absorber at redshift z = 0.89 in front of the quasar PKS 1830–211)[6] using the Atacama Large Millimeter/submillimeter Array (ALMA)[5,6] and the IRAM 30-meter telescope[5]. Furthermore, SH^+ serves as an ideal tracer of high-energy processes in the interstellar medium[5]. Unambiguous identification of submillimeter spectral lines relies on accurate spectroscopic data. Therefore, precise spectral data for SH^+ are not only fundamental for deciphering the evolution of interstellar chemical networks but also provide indispensable key data for revealing the cosmic origin mechanisms of prebiotic molecules.

In the experimental domain, advances in spectroscopic measurement techniques have enabled scientists to conduct high-resolution electronic, rovibrational, and pure rotational spectral studies of the SH^+ ion. These studies cover the ground state ($X^3\Sigma^-$) and four excited states ($a^1\Delta$, $b^1\Sigma^+$, $A^3\Pi$, and $c^1\Pi$) across the submillimeter to ultraviolet regions using gas-phase spectroscopy. However, the reported spectral data remain

incomplete. Regarding the submillimeter and infrared spectra of $X^3\Sigma^-$[7-11], Savage et al.[7] used submillimeter direct absorption/velocity modulation techniques to measure only the $N'' = 0 \rightarrow 1$ transition of SH^+ in the $X^3\Sigma^-(v'' = 0)$ state. Halfen and Ziurys[8] employed submillimeter/terahertz direct absorption spectroscopy. They measured the complete fine structure ($J'' = 0 \leftarrow 1$, $2 \leftarrow 1$, and $1 \leftarrow 1$) of the $N'' = 1 \leftarrow 0$ transition for $X^3\Sigma^-(v'' = 0)$ in the 346–683 GHz frequency range and reported the B_0 and D_0 values for this state. Hovde and Saykally[9] used a laser magnetic resonance (LMR) spectrometer, while Brown et al.[10] utilized velocity-modulated infrared diode laser spectroscopy (VMIDLS). Both groups reported the energy level differences $G_0(1)$, $B_{v''}$, and $D_{v''}$ for $X^3\Sigma^-(v'' = 0, 1)$. Civiš et al.[11] further detected the rovibrational transitions $v'' = 2 \leftarrow 1$, $v'' = 3 \leftarrow 2$, and $v'' = 4 \leftarrow 3$ for this state using VMIDLS. They also extended the reporting of spectral constants for the $X^3\Sigma^-$ state, including the energy level differences $G_0(1–3)$ for $v'' = 1–3$ relative to $v'' = 0$, as well as the $B_{v''}$ and $D_{v''}$ values for $v'' = 0–3$. Milan et al.[12,13] used zero-kinetic-energy pulsed-field ionization (ZEKE-PFI) spectroscopy[12] and two-photon resonance enhanced multiphoton ionization photoelectron spectroscopy (REMPI-PES)[13]. They reported only the B_0 and D_0 for the $a^1\Delta$ state[12], the vibrational level spacings ($\Delta G_{v'+1/2}$) for $a^1\Delta(v' = 0–2)$ and $b^1\Sigma^+(v' = 0, 1)$, alongside the ω_e and $\omega_e x_e$ values for these two states[13]. For the $A^3\Pi \rightarrow X^3\Sigma^-$ ultraviolet and visible emission spectra, Rostas et al.[14] observed the $A^3\Pi \rightarrow X^3\Sigma^-$ system in a custom DC discharge source. By analyzing the (0, 0), (0, 1), and (0, 2) bands, they obtained rotational constants for $A^3\Pi(v' = 0, 1)$ and $X^3\Sigma^-(v'' = 0–2)$. Based on the molecular constants reported by Rostas et al.[14], Horani et al.[15] calculated the band heads, Franck-Condon factors, Einstein A coefficients, and oscillator strengths for the $A^3\Pi$ ($v' = 0, 1$)–$X^3\Sigma^-(v'' = 0–4)$ system, excluding rotational effects. Edwards et al.[16] used coaxial laser/ion beam techniques to supplement observations of rotational transition lines for the $A^3\Pi \rightarrow X^3\Sigma^-(1, 3)$ band. Brzozowski et al.[17] and Gustafsson et al.[18] used high-frequency deflection (HFD) techniques to determine the radiative lifetimes of $A^3\Pi(v' = 0) \rightarrow X^3\Sigma^-(v'' = 0, 1)$[17] and the fluorescence lifetimes of $SH^+(A^3\Pi)$[18], respectively. Using high-resolution laser photofragment spectroscopy, Levick and Sarre[19] detected the (0, 0) band of the $c^1\Pi–b^1\Sigma^+$ system. They fitted only

the B_0 and D_0 for the $b^1\Sigma^+$ and $c^1\Pi$ states. In summary, experimental studies[7-19] have determined partial spectral and molecular constants for the $X^3\Sigma^-$, $a^1\Delta$, $b^1\Sigma^+$, $A^3\Pi$, and $c^1\Pi$ states. However, spectral constants for the individual Ω states after spin-orbit coupling splitting, as well as rovibrational transition data such as the Einstein *A* coefficients ($A_{v'J'\rightarrow v''J''}$), vibrational branching ratios ($R_{v'J'\rightarrow v''J''}$), weighted absorption oscillator strengths ($gf_{v'J'\leftarrow v''J''}$), radiative lifetimes ($\tau_{v'J'}$), and radiative widths (Γ_r) for excited Ω states, have not yet been reported.

With the continuous development and refinement of *ab initio* methods, the accuracy of theoretical calculations for the electronic structures and spectral constants of ten electronic states ($X^3\Sigma^-$, $a^1\Delta$, $b^1\Sigma^+$, $A^3\Pi$, $c^1\Pi$, $2^3\Sigma^-$, $2^3\Pi$, $2^1\Pi$, $3^3\Sigma^-$, and $2^1\Delta$) of the SH^+ ion has significantly improved. Rosmus and Meyer[20] and Senekowitsch et al.[21] obtained spectral constants for the $X^3\Sigma^-$ state using the coupled electron pair approximation (CEPA) method. Park and Sun[22] derived spectral constants for the $X^3\Sigma^-$, $a^1\Delta$, $b^1\Sigma^+$, $A^3\Pi$, and $c^1\Pi$ states using quasi-degenerate many-body perturbation theory (QDMBPT). Using the restricted active space self-consistent field (RASSCF) method, González-Luque et al.[23] reported spectral constants for the $X^3\Sigma^-$ and $A^3\Pi$ states, as well as the lifetimes for $A^3\Pi(v' = 0, 1)$. Subsequently, Stancil et al.[24], Shi et al.[25], Zanchet et al.[26,27], McMillan et al.[28], Song et al.[29], and Zhu et al.[30] employed various methods to obtain spectral constants for the $X^3\Sigma^-$ state. These methods included multi-reference single and double excitation configuration interaction (MRD-CI)[24], coupled cluster theory with single and double excitations and perturbative triple corrections [CCSD(T)][25], internally contracted multi-reference configuration interaction (icMRCI)[26], icMRCI with Davidson correction (+*Q*) (icMRCI+*Q*)[27], MRCI+*Q*[28,29], and explicitly correlated MRCI (MRCI-F12)[30]. In addition, Khadri et al.[31] calculated the potential energy curves for 18 electronic states of the SH^+ ion at the icMRCI+*Q*/cc-pV5Z level. They reported spectral constants for the $X^3\Sigma^-$, $a^1\Delta$, $b^1\Sigma^+$, $A^3\Pi$, $c^1\Pi$, $2^3\Sigma^-$, $2^3\Pi$, $2^1\Pi$, $3^3\Sigma^-$, and $2^1\Delta$ states. Liu et al.[32] calculated the potential energy curves for the $X^3\Sigma^-$, $A^3\Pi$, and $2^3\Pi$ states using MRCI+*Q*/AV5Z theory, thereby determining the spectral and molecular constants for these three states. Xiao et al.[33]

calculated the potential energy curves for 12 Λ-S states and 25 Ω states of the SH^+ ion using the MRCI-F12+*Q* method. They determined the spectral constants for five Λ-S states ($X^3\Sigma^-$, $a^1\Delta$, $b^1\Sigma^+$, $A^3\Pi$, and $c^1\Pi$) and their corresponding nine Ω states. Furthermore, they obtained transition dipole moments, Franck-Condon factors, and radiative lifetimes ($\tau_{v'=0-3}$)for five transition pairs ($a^1\Delta_2 - X^3\Sigma_1^-$, $b^1\Sigma_{0^+}^+ - X^3\Sigma_{0^+}^-$, $b^1\Sigma_{0^+}^+ - X^3\Sigma_1^-$, $A^3\Pi_1 - X^3\Sigma_{0^+}^-$, and $A^3\Pi - X^3\Sigma^-$). However, the aforementioned theoretical studies[20-33] did not comprehensively consider four physical effects that influence the accuracy of potential energy curves and spectral data: core-valence correlation, scalar relativistic effects, spin-orbit coupling, and the complete basis set limit. Moreover, spectral data for certain Λ-S and Ω states, as well as rovibrational transition data for many Ω state transitions-including $A_{v'J'\to v''J''}$, $R_{v'J'\to v''J''}$, wavelengths ($\lambda_{v'J'\to v''J''}$), $gf_{v'J'\leftarrow v''J''}$, $\tau_{v'J'}$ and Γ_r for excited Ω states-have not been reported experimentally or theoretically. In light of this, this study systematically investigated the electronic and rovibrational structures and transition properties of 18 Λ-S states and 35 Ω states of the SH^+ ion using optimized icMRCI+*Q* and quantum mechanical methods.

2 Computational Methods

We performed *ab initio* calculations on the electronic structure of the SH^+ ion under C_{2v} symmetry using the MOLPRO 2010.1 program package[34]. Specifically, we calculated the potential energies of 18 Λ-S states (generated from the first six dissociation limits of the SH^+ ion, see Table 1) using the optimized icMRCI+*Q* method. Since appropriate basis sets and active spaces are critical for improving the accuracy of SA-CASSCF and icMRCI+*Q* calculations[35-38], we determined a suitable active space (6e, 7o) by analyzing the variation of molecular orbital energies with bond length and electron transition behaviors within molecular orbitals obtained via the SA-CASSCF method. This active space includes the six valence electrons and seven molecular orbitals of the SH^+ ion. For the 12 Λ-S states generated from the first three dissociation limits (see Table 1), this active space comprises the 3s, 3p, and 4p orbitals of the S^+ ion and the 1s orbital of the H atom. For the six Λ-S states generated from

the fourth to sixth dissociation limits (see Table 1), this active space includes the 3s, 3p, and 4p orbitals of the S atom. We selected the AV*X*Z (*X* = 5, 6) basis sets[39] for the H atom and the AV(*X*+*d*)Z (*X* = 5, 6) basis sets[40] for the S atom. We then obtained the potential energies of these 18 Λ-S states at the complete basis set limit (denoted as icMRCI+*Q*/56*) using the extrapolation method of Oyeyemi et al.[41]. We obtained the potential energy contributions from scalar relativistic effects (denoted as +SR) using the icMRCI+*Q*/cc-pV5Z-DK[42-44] theory combined with the third-order Douglas-Kroll-Hess (DKH3) approximation[45]. We obtained the potential energy contributions from core-valence correlation effects (denoted as +CV) using the icMRCI+*Q*/cc-pCVTZ[42,46] theory. In frozen-core calculations, only the six valence electrons in the active space (6e, 7o) participated. In all-electron calculations, only the $1s^2$ electrons of S/S^+ were excluded. During the calculations, the step size was 0.002 nm for *R* = 0.0764–0.1744 nm and 0.02 nm for *R* = 0.1764–1.0564 nm. Considering these three physical effects, we constructed the potential energy curves for the 18 Λ-S states at the icMRCI+*Q*/56*+SR+CV level (see Figure 1). We obtained the potential energy contributions from spin-orbit coupling effects (denoted as +SOC) using the full Breit-Pauli spin-orbit coupling operator ($\hat{H}_{SO}$)[47] combined with the all-electron icMRCI+*Q*/cc-pCV5Z theory. Considering all four physical effects, we obtained precise potential energy curves for the 35 Ω states at the icMRCI+*Q*/56*+SR+CV+SOC level (see Figure 2). Additionally, at the all-electron icMRCI/cc-pCV5Z+SOC level, we obtained the transition dipole moment curves for 12 systems among seven Ω states [$X^3\Sigma^-_{0^+}$, $X^3\Sigma^-_1$, $(1)2^{1st\ well}(\upsilon' = 0–8)$, $(2)0^+(\upsilon' = 0–5)$, $(2)2^{1st\ well}(\upsilon' = 0–2)$, $(2)1^{1st\ well}(\upsilon' = 0–2)$, and $(3)0^+(\upsilon' = 0–2)$] that are less perturbed by other Ω states, as shown in Figure 3.

Table 1 Dissociation relationships for the eighteen Λ-S states of the SH^+ ion.

离解极限	Λ-S态	能量/cm^{-1}		
		本文	实验[49]	本文与实验[49]的偏差
$S^+(^4S_u) + H(^2S_g)$	$X^3\Sigma^-$, $1^5\Sigma^-$	0	0	0
$S^+(^2D_u) + H(^2S_g)$	$1^1\Sigma^-$, $2^3\Sigma^-$, $c^1\Pi$, $A^3\Pi$, $a^1\Delta$, $1^3\Delta$	14717	14869[a)]	152(1.022%)
$S^+(^2P_u) + H(^2S_g)$	$b^1\Sigma^+$, $1^3\Sigma^+$, $2^1\Pi$, $2^3\Pi$	24289	24548[a)]	259(1.055%)
$S(^3P_g) + H^+(^1S_g)$	$3^3\Sigma^-$, $3^3\Pi$	26662	26605[a)]	57(0.214%)
$S(^1D_g) + H^+(^1S_g)$	$2^1\Sigma^+$, $3^1\Pi$, $2^1\Delta$	35208	35358	150(0.424%)
$S(^1S_g) + H^+(^1S_g)$	$3^1\Sigma^+$	48189	48300	111(0.230%)

Note: a) denotes the arithmetic mean of the *J* energy levels.

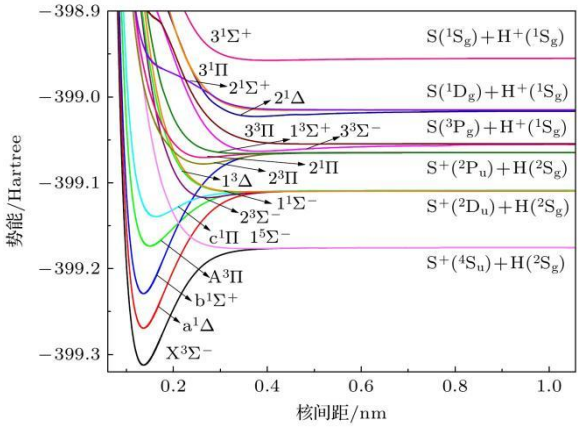

Fig. 1 Potential energy curves of the eighteen Λ-S states for the SH^+ ion obtained using the icMRCI+*Q*/56*+SR+CV method.

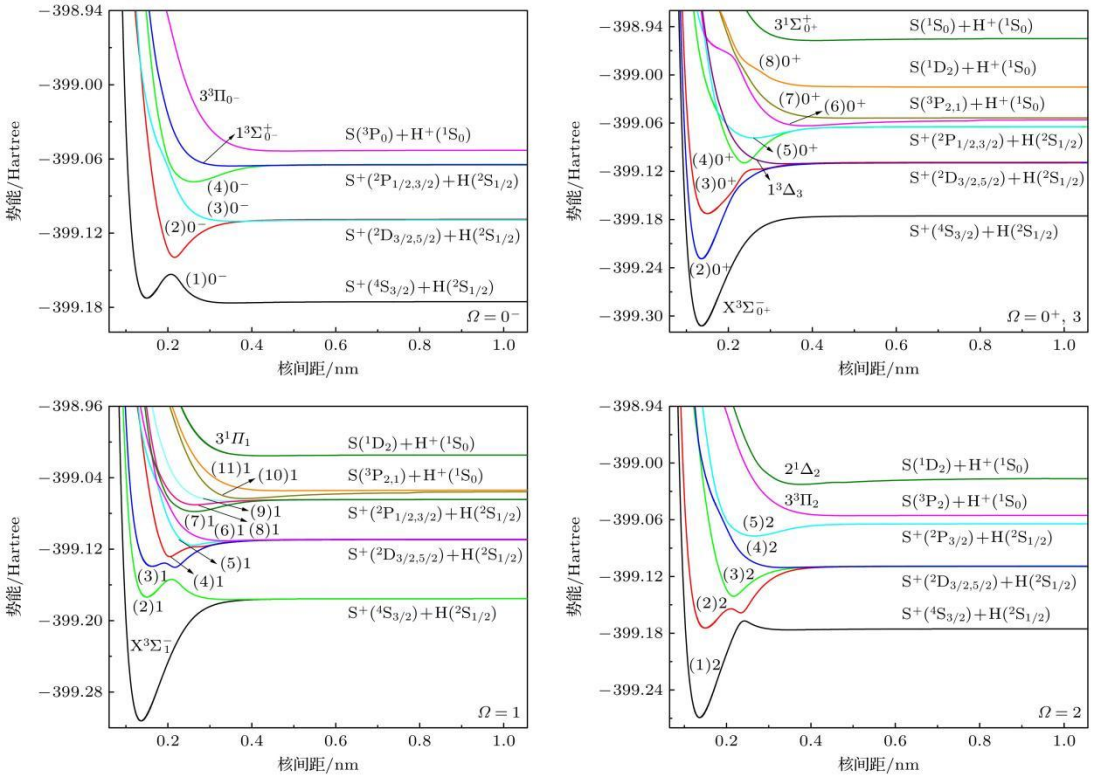

Fig. 2 Potential energy curves of the thirty-five Ω states for the SH^+ ion obtained using the icMRCI+*Q*/56*+SR+CV+SOC method.

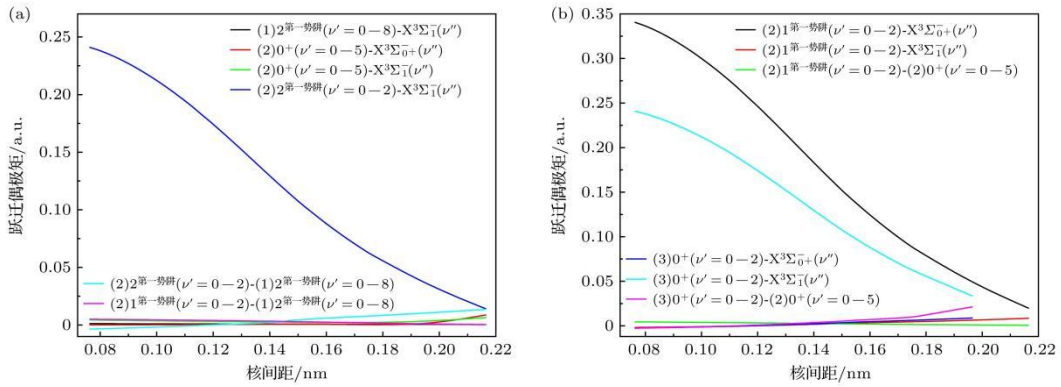

Fig. 3 Transition dipole moment curves for the twelve transition systems of the SH^+ ion.

Based on the potential energy curves in Figures 1 and 2 and the transition dipole moment curves for the 12 systems in Figure 3, we solved the Schrödinger equation for the nuclear motion of the SH^+ ion using the LEVEL 8.2 program[48]. By employing Eqs. (1)—(4), we obtained the spectroscopic and molecular constants for 16 bound or weakly bound Λ-S states ($X^3\Sigma^-$, $a^1\Delta$, $b^1\Sigma^+$, $1^5\Sigma^-$, $A^3\Pi$, $c^1\Pi$, $2^3\Sigma^-$, $1^3\Delta$, $1^1\Sigma^-$, $2^3\Pi$, $2^1\Pi$, $1^3\Sigma^+$, $3^3\Sigma^-$, $2^1\Delta$, $3^1\Pi$, and $3^1\Sigma^+$) and 30 Ω states of the SH^+ ion. Furthermore, we determined rovibrational transition data for the 12 systems, including $A_{v'J'\to v''J''}$, $R_{v'J'\to v''J''}$, transition wavenumbers ($\tilde{v}$), $gf_{v'J'\leftarrow v''J''}$, and $\lambda_{v'J'\to v''J''}$. We also calculated the $\tau_{v'J'}$ and Γ_r values for five excited Ω states: (1)$2^{1st\ well}$ (v' = 0–8, J' = 2, +), (2)0^+ (v' = 0–5, J' = 0, +), (2)$2^{1st\ well}$ (v' = 0–2, J' = 2, +), (2)$1^{1st\ well}$ (v' = 0–2, J' = 1, +), and (3)0^+ (v' = 0–2, J' = 0, +).

We calculated $R_{v'J'\to v''J''}$, $gf_{v'J'\leftarrow v''J''}$, $\tau_{v'J'}$, and Γ_r using the following formulas:

$$R_{v'J'\to v''J''} = A_{v'J'\to v''J''} \Big/ \sum_{v''} A_{v'J'\to v''J''}, \quad (1)$$

$$gf_{v'J'\leftarrow v''J''} = 1.4991938\frac{2J'+1}{\tilde{\nu}^2}A_{v'J'\rightarrow v''J''}, \quad (2)$$

$$\tau_{v'J'} = \frac{1}{A_{v'J'}} = \frac{1}{\sum_i A_{i,v'J'}}, \quad (3)$$

$$\Gamma_\gamma = \frac{1}{(2\pi c\tau_{v'J'})}. \quad (4)$$

In Eq. (2), $g = 2J''+1$; in Eq. (3), $A_{i,v'J'}$ denotes the total Einstein A coefficient for emission transitions from a given upper $v'J'$ level to all $v''J''$ levels of the ith lower state.

Based on the icMRCI+*Q*/56*+SR+CV theory, we also obtained the energies corresponding to the six dissociation limits of the SH^+ ion (see Table 1). As shown in Table 1, our results agree well with the measured values reported by Sansonetti and Martin[49].

3 Results and Discussion

3.1 Spectroscopic and Molecular Constants of the 16 Λ-S States

Figure 1 shows that among the 18 Λ-S states of this ion, only the $3^3\Pi$ and $2^1\Sigma^+$ states are repulsive. Table 2 presents the spectral constants, dominant valence electron configurations at the equilibrium internuclear distance, experimental data[5,11-14,19], and other theoretical results[20-33] for the remaining 16 bound or weakly bound Λ-S states obtained in this study.

Overall, under the icMRCI+*Q*/56*+SR+CV theory, the spectral constants for the $X^3\Sigma^-$, $a^1\Delta$, $b^1\Sigma^+$, and $A^3\Pi$ states show the highest agreement with existing experimental data[5,11,13,14] (see Table 2). Based on this, the following section analyzes and discusses the relevant spectral constants derived from the icMRCI+*Q*/56*+SR+CV theory.

The ground electronic configuration of the SH^+ ion forms the $X^3\Sigma^-$, $a^1\Delta$, and $b^1\Sigma^+$ states (as listed in Table 2). The potential well depths for these three states are 30037.08, 35122.31, and 36025.66 cm^{-1}, respectively, supporting 22, 25, and 26

vibrational states.

Table 2 Spectral constants of sixteen Λ-S states for the SH^+ ion.

Table 2 Spectral constants of sixteen Λ-S states for the SH⁺ ion.

Λ-S态	来源	T_e/cm^{-1}	R_e/nm	ω_e/cm^{-1}	$\omega_e x_e$/cm^{-1}	B_e/cm^{-1}	$10^2\alpha_e$/cm^{-1}	D_e/eV	R_e处主要的价电子组态[a]
$X^3\Sigma^-$	icMRCI+Q/AV5Z*	0	0.13653	2533.81	44.1544	9.20075	24.6556	3.6934	
	icMRCI+Q/AV6Z*	0	0.13652	2534.52	44.1089	9.20232	24.6607	3.7018	
	icMRCI+Q/56*	0	0.13652	2535.42	44.0114	9.20309	24.6573	3.7163	
	icMRCI+Q/56*+SR	0	0.13652	2532.15	43.9322	9.20297	24.6422	3.7069	
	icMRCI+Q/56*+CV	0	0.13620	2550.85	43.3195	9.23974	24.2123	3.7336	
	icMRCI+Q/56*+SR+CV	0	0.13620	2547.58	43.2366	9.23968	24.1939	3.7241	$4\sigma^2 5\sigma^2 2\pi^2 6\sigma^0 3\pi^0$(92.14%
	实验[5]	0	—	2547.49	49.4293	9.27625	28.6109		
	实验[11]	0	0.13636	2547.17	49.0827	9.27634	28.6152		
	实验[14]	0	0.13638	2547.7	49.3	9.2759	28.49	3.70	
	理论[20]	0	0.1368	2566.1	54.5	9.21	28.4		
	理论[21]	0	0.1366	2542	48	9.24	28.4		
	理论[22]	0	0.13568	2616.8	51.2	9.29	23.9	3.45	
	理论[23]	0	0.1367	2540	51.7	9.24	30	3.46	
	理论[24]	0	0.13658	2565	—	—	—	3.52	
	理论[25]	0	0.13644	2556.43	49.290	9.2677	28.90	3.6912	
	理论[26]	0	0.1365	—	—	—	—	3.72	
	理论[27]	0	0.1368	2532	—	—	—	3.67	
	理论[28]	0	0.13547	2601.1	54.1	—	—	3.843	
	理论[29]	0	0.13633	—	—	—	—	3.6803	
	理论[30]	0	0.13650	2547.4	51.89	9.259	28.94	3.691	
	理论[31]	0	0.1361	2555.2	49.00	9.279	28.5	3.6449	
	理论[32]	0	0.13640	2544.7	48.4	9.6380	29.65	3.7028	
	理论[33]	0	0.13624	2554.61	48.7851	9.2947	—	3.636	
$a^1\Delta$	icMRCI+Q/AV5Z*	9427.53	0.13639	2549.08	42.8901	9.17847	23.4311	4.3342	
	icMRCI+Q/AV6Z*	9392.42	0.13638	2549.69	42.9044	9.18005	23.4588	4.3403	
	icMRCI+Q/56*	9328.11	0.13639	2550.51	42.9245	9.18088	23.4961	4.3504	
	icMRCI+Q/56*+SR	9331.40	0.13638	2547.38	42.8173	9.18050	23.4554	4.3413	
	icMRCI+Q/56*+CV	9437.63	0.13613	2560.49	43.1082	9.21117	23.5083	4.3637	
	icMRCI+Q/56*+SR+CV	9441.14	0.13612	2557.36	43.0018	9.21085	23.4673	4.3546	$4\sigma^2 5\sigma^2 2\pi^2 6\sigma^0 3\pi^0$(91.74%)
	实验[13]	—	—	2556	45	9.186[b]			
	理论[22]	10727.17	0.13632	2706.7	26.76	9.21	23	4.417	
	理论[31]	10186.78	0.1362	2567.2	47.48	9.285	28.0	4.2597	
	理论[33]	9745.35	0.13606	2555.05	42.2261	9.3192	—	4.333	
$b^1\Sigma^+$	icMRCI+Q/AV5Z*	18488.98	0.13632	2558.48	43.8204	9.21435	24.5263	4.4530	
	icMRCI+Q/AV6Z*	18441.14	0.13632	2558.83	43.8258	9.21535	24.5459	4.4584	
	icMRCI+Q/56*	18353.79	0.13633	2559.15	43.8284	9.21502	24.5683	4.4674	
	icMRCI+Q/56*+SR	18378.81	0.13633	2556.04	43.7294	9.21476	24.5366	4.4579	
	icMRCI+Q/56*+CV	18265.34	0.13608	2569.62	44.0495	9.24708	24.5960	4.4761	
	icMRCI+Q/56*+SR+CV	18290.36	0.13607	2566.51	43.9509	9.24688	24.5638	4.4666	$4\sigma^2 5\sigma^2 2\pi^2 6\sigma^0 3\pi^0$(89.14%)
	实验[13]	—	—	2563	47	9.1642[c]			
	理论[22]	22502.86	0.13579	2705.50	24.02	9.29	23.4	4.19	
	理论[31]	18881.43	0.1362	2576.7	47.34	9.298	27.9	4.3663	
	理论[33]	18564.78	0.13592	2570.63	42.7640	9.3378	—	4.440	
$1^5\Sigma^-$	icMRCI+Q/56*+SR+CV	29811.02	0.34974	166.312	38.3324	1.42327	32.1284	0.0287	$4\sigma^2 5\sigma^1 2\pi^2 6\sigma^1 3\pi^0$(93.37%)
$A^3\Pi$	icMRCI+Q/AV5Z*	30213.98	0.14954	1693.24	44.9194	7.66940	32.8770	1.8100	
	icMRCI+Q/AV6Z*	30198.83	0.14954	1693.72	44.9039	7.66954	32.8775	1.8135	
	icMRCI+Q/56*	30168.11	0.14956	1694.20	44.8320	7.66819	32.8600	1.8196	
	icMRCI+Q/56*+SR	30275.65	0.14989	1678.82	43.9295	7.63172	32.4899	1.7971	
	icMRCI+Q/56*+CV	30336.22	0.14939	1693.51	46.5230	7.68158	33.4786	1.7840	
	icMRCI+Q/56*+SR+CV	30444.20	0.14972	1677.76	45.5651	7.64464	33.0934	1.7614	$4\sigma^2 5\sigma^1 2\pi^3 6\sigma^0 3\pi^0$(89.47%)
	实验[14]	30345.05	0.15008	1672.4	47.6	7.656	35.73	1.7767	
	理论[22]	33310.68	0.14859	1775.8	61.1	7.74	20.0	1.62	
	理论[23]	30595	0.1502	1660	49.1	7.65	40	1.64	
	理论[31]	30853.11	0.1497	1697.2	56.59	7.691	38.2	1.7095	
	理论[32]	—	0.14920	1676.8	44.1	8.5531	40.99	1.7842	
	理论[33]	30518.99	0.14952	1680.79	40.9797	7.7107	—	1.760	
$c^1\Pi$	icMRCI+Q/56*+SR+CV	37969.11	0.16284	1276.56	37.6672	6.43429	25.2501	0.8285	$4\sigma^2 5\sigma^1 2\pi^3 6\sigma^0 3\pi^0$(84.43%),
	实验[19]	—	—	—	—	6.2286[c]			$4\sigma^2 5\sigma^0 2\pi^3 6\sigma^1 3\pi^0$(4.89%)
	理论[22]	42102.12	0.16129	1246.0	201.4	6.51	11	0.524	
	理论[31]	38424.24	0.1651	1224.5	46.60	6.288	32.1	0.7845	
	理论[33]	37999.62	0.16344	1290.00	62.0699	6.4602	—	1.017	

$2^3\Sigma^-$	icMRCI+Q/56*+SR+CV	42719.86	0.26952	658.975	23.3895	2.35918	9.10885	0.2249	$4\sigma^25\sigma^12\pi^26\sigma^13\pi^0$(80.31%),
	理论[31]	43142.58	0.2707	616.4	23.08	2.314	6.7	0.1846	$4\sigma^25\sigma^22\pi^26\sigma^03\pi^0$(12.13%)
$1^3\Delta$	icMRCI+Q/56*+SR+CV	44275.28	0.32574	244.964	83.1818	1.59008	43.1803	0.0364	$4\sigma^25\sigma^12\pi^26\sigma^13\pi^0$(92.67%)
$1^1\Sigma^-$	icMRCI+Q/56*+SR+CV	44315.66	0.35878	158.196	38.5784	1.35631	32.5154	0.0260	$4\sigma^25\sigma^12\pi^26\sigma^13\pi^0$(92.73%)
$2^3\Pi$	icMRCI+Q/56*+SR+CV	51355.97	0.26273	605.199	10.4554	2.43899	24.8410	0.3751	$4\sigma^25\sigma^22\pi^16\sigma^13\pi^0$(73.37%),
	理论[31]	51692.05	0.2620	600.5	15.96	2.484	4.9	0.2998	$4\sigma^25\sigma^12\pi^36\sigma^03\pi^0$(15.35%),
	理论[32]	—	0.25858	634.4	20.2	2.5483	1.15	0.3584	$4\sigma^25\sigma^02\pi^36\sigma^13\pi^0$(2.22%)
$2^1\Pi$	icMRCI+Q/56*+SR+CV	53018.27	0.26294	535.536	42.9774	2.48850	17.5469	0.1690	$4\sigma^25\sigma^22\pi^16\sigma^13\pi^0$(67.74%), $4\sigma^25\sigma^02\pi^36\sigma^13\pi^0$(11.55%),
	理论[31]	53111.59	0.2667	500.2	13.68	2.389	10.0	0.1447	$4\sigma^25\sigma^12\pi^36\sigma^03\pi^0$(11.39%)
$1^3\Sigma^+$	icMRCI+Q/56*+SR+CV	54092.38	0.35122	164.554	36.6728	1.40980	31.4536	0.0283	$4\sigma^25\sigma^12\pi^26\sigma^13\pi^0$(91.36%)
$3^3\Sigma^-$	icMRCI+Q/56*+SR+CV	54638.43	0.37940	341.127	20.0194	1.19833	7.65666	0.2327	$4\sigma^25\sigma^12\pi^26\sigma^13\pi^0$(70.69%),
	理论[31]	56539.44	0.3841						$4\sigma^25\sigma^22\pi^26\sigma^03\pi^0$(13.59%)
$2^1\Delta$	icMRCI+Q/56*+SR+CV	63541.86	0.37388	347.292	2.55690	1.23329	6.96309	0.1668	$4\sigma^25\sigma^12\pi^26\sigma^13\pi^0$(70.93%),
	理论[31]	65564.78	0.3669						$4\sigma^25\sigma^22\pi^26\sigma^03\pi^0$(14.07%)
$3^1\Pi$	icMRCI+Q/56*+SR+CV	65151.48	0.42904	131.057	33.7213	0.93379	19.5468	0.0204	$4\sigma^15\sigma^22\pi^36\sigma^03\pi^0$(89.79%)
$3^1\Sigma^+$	icMRCI+Q/56*+SR+CV	77904.50	0.40229	182.037	20.4757	1.06690	12.7060	0.0668	$4\sigma^25\sigma^12\pi^26\sigma^13\pi^0$(66.52%),
									$4\sigma^25\sigma^22\pi^26\sigma^03\pi^0$(13.62%)

注: a)表示小括号里是组态函数系数的平方值; b)表示实验[12]的B_0值; c)表示实验[19]的B_0值.

The $G_0(\upsilon'' = 1–3)$ values [2459.95, 4830.22, and 7108.68 cm^{-1}] for the $X^3\Sigma^-$ state in this study agree well with experimental measurements[9-11,14]. They are slightly larger than the $G_0(\upsilon'' = 1–3)$ values reported by Rostas et al.[14] by 10.71 cm^{-1} (0.437%), 29.18 cm^{-1} (0.608%), and 52.95 cm^{-1} (0.751%), respectively. The calculated $B_{\upsilon''}$ (9.15997, 8.87823, 8.59698, 8.31643 cm^{-1}) and $D_{\upsilon''}$ (4.871×10^{-4}, 4.828×10^{-4}, 4.779×10^{-4}, 4.749×10^{-4} cm^{-1}) for $X^3\Sigma^-(\upsilon'' = 0–3)$ in this work also align well with corresponding experimental values[8-11,14]. Specifically, the $B_{\upsilon''}$ values for $\upsilon'' = 0–3$ reported by Civiš et al.[11] (9.13343, 8.84828, 8.56422, 8.28080 cm^{-1}) are smaller than those in this study by 0.02654 cm^{-1} (0.291%), 0.02995 cm^{-1} (0.338%), 0.03276 cm^{-1} (0.383%), and 0.03583 cm^{-1} (0.433%), respectively. The deviations of the calculated $D_{\upsilon''}$ ($\upsilon'' = 0–3$) from the corresponding values reported by Rostas et al.[14] (4.912×10^{-4}, 4.813×10^{-4}, 4.749×10^{-4}, 4.721×10^{-4} cm^{-1}) are 4.10×10^{-6} cm^{-1} (0.835%), 1.50×10^{-6} cm^{-1} (0.312%), 3.00×10^{-6} cm^{-1} (0.632%), and 2.80×10^{-6} cm^{-1} (0.593%), respectively. As shown in Table 2, the R_e, ω_e, B_e, and D_e values for the $X^3\Sigma^-$ state obtained in this study are also quite consistent with measured values[5,11,14]. Specifically, the deviations of R_e and D_e from the values of Rostas et al.[14] are 0.00018 nm (0.132%) and 0.0241 eV (0.651%), respectively. The deviations of ω_e and B_e from the most recent experimental data[5] are 0.09 cm^{-1} (0.004%) and 0.03657 cm^{-1} (0.394%), respectively. Only the theoretical R_e values[25,26,29,30,32,33], theoretical B_e values[21-23,25,30,31,33], and theoretical D_e

values[25,26,29,30,32] are closer to the experimental values[5,11,14] than the results of this study.

The $\Delta G_{v'+1/2}$(v' = 0–2) [2471.18, 2384.67, 2297.82 cm^{-1}] and B_0 (9.16964 cm^{-1}) for the $a^1\Delta$ state obtained in this study agree well with the experimental measurements of Milan et al.[12,13]. The deviations of $\Delta G_{v'+1/2}$(v' = 0–2) from the corresponding values (2479, 2367, and 2297 cm^{-1}) reported by Milan et al.[13] are 7.82 cm^{-1} (0.315%), 17.67 cm^{-1} (0.747%), and 0.82 cm^{-1} (0.036%), respectively. The obtained B_0 is 0.01636 cm^{-1} (0.178%) smaller than the experimental datum (9.186 cm^{-1}) of Milan et al.[12]. As shown in Table 2, the ω_e of the $a^1\Delta$ state in this study is only 1.36 cm^{-1} (0.053%) larger than the experimental result of Milan et al.[13]. Furthermore, the $\omega_e x_e$ in this study is closer to the experimental value of Milan et al.[13] than the theoretical values[22,31,33].

The $\Delta G_{v'+1/2}$(v' = 0–1) values for the $b^1\Sigma^+$ state in this study are 2478.67 and 2390.90 cm^{-1}, respectively. These are 9.67 cm^{-1} (0.392%) and 16.90 cm^{-1} (0.712%) larger than the experimental values (2469 and 2374 cm^{-1}) of Milan et al.[13], respectively. The obtained B_0 (9.17952 cm^{-1}) and D_0 (4.823×10^{-4} cm^{-1}) are only 0.01532 cm^{-1} (0.167%) and 3.00×10^{-7} cm^{-1} (0.062%) larger than the experimental results (9.1642 cm^{-1} and 4.82×10^{-4} cm^{-1}) of Levick and Sarre[19], respectively. The ω_e obtained in this study is also only 3.51 cm^{-1} (0.137%) larger than the experimental measurement of Milan et al.[13] (see Table 2).

The first excited electronic configuration of SH^+ originates from single-electron excitation from the 5σ orbital to the 2π orbital. This configuration generates the $A^3\Pi$ and $c^1\Pi$ molecular states (see Table 2). The potential well depths for these two states are 14207.03 and 6682.78 cm^{-1}, respectively, supporting 16 and 11 vibrational states. As shown in Table 2, the deviations of the T_e, R_e, ω_e, B_e, and D_e values for the $A^3\Pi$ state obtained in this study from the corresponding values of Rostas et al.[14] are 99.15 cm^{-1} (0.327%), 0.00036 nm (0.240%), 5.36 cm^{-1} (0.321%), 0.01136 cm^{-1} (0.148%), and 0.0153 eV (0.861%), respectively, indicating good agreement. Only the R_e and B_e values of Gonzâlez-Luque et al.[23] and the ω_e and D_e values of Liu et al.[32] are slightly closer to the experimental measurements of Rostas et al.[14] than the results of this study. The calculated T_{00}, T_{10}, and T_{13} values are 30008.76, 31595.52, and 24486.84 cm^{-1},

respectively. These are 100.93 cm^{-1} (0.338%), 110.45 cm^{-1} (0.351%), and 57.50 cm^{-1} (0.235%) larger than the experimental values of Rostas et al.[14] and Edwards et al.[16], respectively. The calculated $B_{v'}$ values (7.47891, 7.14589 cm^{-1}) for the vibrational states $v' = 0, 1$ are only 0.00147 cm^{-1} (0.020%) and 0.02579 cm^{-1} (0.362%) larger than the corresponding values (7.47744, 7.12010 cm^{-1}) of Rostas et al.[14], respectively. The calculated $D_{v'}$ ($v' = 0, 1$) values are 6.311×10^{-4} and 6.188×10^{-4} cm^{-1}, respectively. Their deviations from the values of Rostas et al.[14] (6.312×10^{-4}, 6.129×10^{-4} cm^{-1}) are 1.00×10^{-7} cm^{-1} (0.016%) and 5.90×10^{-6} cm^{-1} (0.963%), respectively.

The B_0 (6.29936 cm^{-1}) and D_0 (6.641×10^{-4} cm^{-1}) for the $c^1\Pi$ state obtained in this study are only 0.07076 cm^{-1} (1.136%) and 1.00×10^{-7} cm^{-1} (0.015%) larger than the corresponding experimental values (6.2286 cm^{-1} and 6.64×10^{-4} cm^{-1}) of Levick and Sarre[19], respectively.

The second excited electronic configuration of the SH^+ ion is formed by the transition of an electron from the 2π orbital to the 6σ orbital, resulting in the $2^3\Pi$ and $2^1\Pi$ molecular states (see Table 2). The potential well depths for these two states are 3025.24 and 1362.94 cm^{-1}, respectively, supporting 9 and 6 vibrational states. The third excited configuration originates from two-electron excitation out of the 5σ orbital into the 2π orbital, resulting in the $2^1\Sigma^+$ molecular state (repulsive state). The fourth excited electronic configuration arises from the excitation of an electron from the 5σ orbital to the 6σ orbital, resulting in the $1^5\Sigma^-$, $2^3\Sigma^-$, $1^3\Delta$, $1^1\Sigma^-$, $1^3\Sigma^+$, $3^3\Sigma^-$, $2^1\Delta$, and $3^1\Sigma^+$ states. The potential well depths for these eight states are 231.77, 1814.18, 293.44, 210.04, 228.47, 1876.73, 1345.64, and 538.81 cm^{-1}, respectively, supporting 4, 6, 4, 3, 3, 14, 6, and 7 vibrational states. The fifth excited electronic configuration is formed by the transition of an electron from the 4σ orbital to the 2π orbital, resulting in the repulsive $3^3\Pi$ state and the weakly bound $3^1\Pi$ state.

3.2 Spectral Constants of the 30 Ω States

After including spin-orbit coupling effects, the first through sixth dissociation limits of the SH^+ ion further split into 10 dissociation limits. Table 3 lists the 35 Ω states generated by these 10 dissociation limits, the dissociation limit energy intervals

calculated in this study, the measured values[49], and the theoretical values[33]. Table 4 lists the spectral constants for the 30 bound/weakly bound Ω states and the composition of the Ω states at the equilibrium internuclear distance. As shown in Table 3, the dissociation limit energy intervals obtained in this study remain consistent with the measured values of Sansonetti and Martin[49].

Table 3. Dissociation relationships for the thirty-five Ω states of SH^+ ion.

原子态	Ω态	能量/cm^{-1}			
		本文	实验[49]	理论[33]	本文与实验[49]的偏差
$S^+(^4S_{3/2}) + H(^2S_{1/2})$	2, 1(2), 0^+, 0^-	0	0	0	0
$S^+(^2D_{3/2}) + H(^2S_{1/2})$	2, 1(2), 0^+, 0^-	14683.27	14852.94	14312	169.67(1.142%)
$S^+(^2D_{5/2}) + H(^2S_{1/2})$	3, 2(2), 1(2), 0^+, 0^-	14749.70	14884.73	14340	135.03(0.907%)
$S^+(^2P_{1/2}) + H(^2S_{1/2})$	0^-, 0^+, 1	24300.85	24524.83	24109	223.98(0.913%)
$S^+(^2P_{3/2}) + H(^2S_{1/2})$	2, 1(2), 0^+, 0^-	24334.18	24571.54	24141	237.36(0.966%)
$S(^3P_2) + H^+(^1S_0)$	2, 1, 0^+	26163.12	26119.65		43.47(0.166%)
$S(^3P_1) + H^+(^1S_0)$	1, 0^+	26569.71	26515.71		54.00(0.204%)
$S(^3P_0) + H^+(^1S_0)$	0^-	26753.83	26693.29		60.54(0.227%)
$S(^1D_2) + H^+(^1S_0)$	2, 1, 0^+	35302.53	35358.26		55.73(0.158%)
$S(^1S_0) + H^+(^1S_0)$	0^+	47912.93	48299.60		386.67(0.801%)

Table 4. Spectral constants of the thirty Ω states for SH^+ ion.

Ω态	T_e/cm^{-1}	R_e/nm	ω_e/cm^{-1}	$\omega_e x_e$/cm^{-1}	B_e/cm^{-1}	$10^2\alpha_e$/cm^{-1}	D_e/eV	在R_e附近主要的Λ-S态/%
$X^3\Sigma^-_{0+}$	0	0.13620	2547.56	43.2445	9.23971	24.2005	3.7247	$X^3\Sigma^-$(99.94), $b^1\Sigma^+$(0.06)
$X^3\Sigma^-_1$	10.75	0.13620	2547.48	43.2383	9.23948	24.1901	3.7234	$X^3\Sigma^-$(100.00)
(1)2^{第一势阱}	9450.80	0.13612	2573.87	46.0128	9.28908	26.3924	2.8723	$a^1\Delta$(100.00)
(1)2^{第二势阱}	29815.19	0.34963	166.454	33.3357	1.42382	32.1592	0.0288	$1^5\Sigma^-$(99.96), $2^3\Pi$(0.04)
(2)0$^+$	18309.67	0.13608	2574.94	44.1139	9.27761	24.0330	3.2512	$b^1\Sigma^+$(99.90), $X^3\Sigma^-$(0.06), $A^3\Pi$(0.04)
(2)2^{第一势阱}	30240.09	0.14972	1696.85	49.7033	7.65112	25.4811	1.7760	$A^3\Pi$(99.98), $a^1\Delta$(0.02)
(2)2^{第二势阱}	32806.85	0.23880	2509.39	—	3.16915	—	1.4580	$a^1\Delta$(77.40), $1^5\Sigma^-$(22.60)
(2)1^{第一势阱}	30450.79	0.14974	1695.16	47.9175	7.63611	21.9436	0.5737	$A^3\Pi$(99.92), $c^1\Pi$(0.08)
(2)1^{第二势阱}	29815.41	0.34974	166.287	33.2853	1.42357	32.1552	0.0287	$1^5\Sigma^-$(99.96), $2^3\Pi/1^3\Sigma^+$(0.02)
(3)0$^+$	30673.77	0.14974	1694.38	53.4587	7.70022	33.8758	1.7345	$A^3\Pi$(100.00)
(1)0$^-$ ^{第一势阱}	30678.82	0.14972	1694.69	52.0127	7.68855	36.0301	0.5236	$A^3\Pi$(99.96), $1^3\Sigma^+$(0.04)
(1)0$^-$ ^{第二势阱}	29815.41	0.34973	166.291	33.3016	1.42343	32.1416	0.0287	$1^5\Sigma^-$(99.96), $1^3\Sigma^+$(0.04)
(3)2	36841.67	0.21486	2156.09	105.219	3.74364	2.85076	0.9665	$A^3\Pi$(98.14), $1^5\Sigma^-$(1.80), $a^1\Delta$(0.06)
(2)0$^-$	37187.56	0.21388	2060.02	79.4391	3.77473	2.45528	0.9271	$A^3\Pi$(99.64), $1^5\Sigma^-$(0.36)
(3)1^{第一势阱}	37987.11	0.16284	1300.51	—	6.66115	—	0.8118	$c^1\Pi$(99.88), $A^3\Pi$(0.12)
(3)1^{第二势阱}	37024.27	0.21546	2152.30	—	3.71384	—	0.9312	$A^3\Pi$(99.33), $1^5\Sigma^-$(0.40), $c^1\Pi$(0.27)
(4)1	39384.28	0.19998	2690.28	495.643	4.32746	19.2305	0.6441	$c^1\Pi$(99.76), $A^3\Pi$(0.22), $2^3\Sigma^-$(0.02)
(5)1	42930.77	0.25650	1185.01	332.068	2.78170	50.8417	0.2116	$c^1\Pi$(97.84), $2^3\Sigma^-$(1.62), $A^3\Pi$(0.44), $1^3\Delta/2^3\Pi$(0.04), $1^3\Sigma^+$(0.02)
(4)0$^+$	43840.50	0.23710	1966.06	92.9619	3.06675	0.09380	1.3080	$2^3\Sigma^-$(99.44), $b^1\Sigma^+$(0.52), $A^3\Pi$(0.04)
(6)1	44277.03	0.32579	288.476	80.0397	1.55515	28.5282	0.0485	$1^3\Delta$(99.48), $c^1\Pi$(0.24), $A^3\Pi$(0.12), $2^3\Pi/2^1\Pi$(0.08)
(4)2	44277.91	0.32581	287.588	71.7403	1.54796	33.6822	0.0376	$1^3\Delta$(99.72), $A^3\Pi$(0.16), $2^3\Pi$(0.12)
$1^3\Delta_3$	44278.35	0.32626	242.418	83.0728	1.56957	40.1452	0.0360	$1^3\Delta$(99.78), $c^1\Pi$(0.09), $A^3\Pi$(0.05), $2^3\Pi/2^1\Pi$(0.04)
(3)0$^-$	44313.07	0.35846	160.048	35.4678	1.35876	29.6762	0.0272	$1^1\Sigma^-$(99.81), $A^3\Pi$(0.08), $1^3\Sigma^+$(0.07), $2^3\Pi$(0.04)
(4)0$^-$	51249.52	0.26088	619.367	10.2581	2.48406	1.25983	0.3923	$2^3\Pi$(99.78), $1^1\Sigma^-/1^3\Sigma^+$(0.09), $A^3\Pi$(0.04)
(5)0$^+$	51250.18	0.26088	621.277	11.7401	2.48164	1.38666	0.3923	$2^3\Pi$(99.92), $A^3\Pi$(0.04), $b^1\Sigma^+/2^3\Sigma^-$(0.02)

Table 4 (continued). Spectral constants of the thirty Ω states for SH^+ ion.

Ω态	T_e/cm^{-1}	R_e/nm	ω_e/cm^{-1}	$\omega_e x_e$/cm^{-1}	B_e/cm^{-1}	$10^2\alpha_e$/cm^{-1}	D_e/eV	在R_e附近主要的Λ-S态/%
(7)1	51382.08	0.26228	605.316	10.4383	2.48928	2.66297	0.3774	$2^3\Pi$(98.88), $2^1\Pi$(0.82), $1^3\Delta$(0.16), $c^1\Pi$(0.06), $1^3\Sigma^+$(0.04), $2^3\Sigma^-/1^5\Sigma^-$(0.02)
(5)2	51522.11	0.26449	589.971	9.18912	2.39668	3.44104	0.3601	$2^3\Pi$(99.70), $1^3\Delta$(0.18), $A^3\Pi/1^1\Delta/1^5\Sigma^-$(0.04)
(8)1	53062.60	0.26822	536.821	45.1547	2.48197	17.1823	0.1675	$2^1\Pi$(98.90), $2^3\Pi$(0.80), $1^3\Delta$(0.20), $2^3\Sigma^-$(0.10)
$1^3\Sigma^+_1$	54128.37	0.35107	174.011	49.6721	1.43237	35.9687	0.0277	$1^3\Sigma^+$(99.70), $1^3\Delta$(0.08), $2^1\Pi$(0.06), $c^1\Pi/A^3\Pi$(0.05), $3^3\Sigma^-$(0.04), $1^5\Sigma^-$(0.02)
$1^3\Sigma^+_{0-}$	54128.46	0.35110	168.756	44.2580	1.42849	35.8142	0.0277	$1^3\Sigma^+$(99.79), $A^3\Pi$(0.12), $1^1\Sigma^-$(0.07), $1^5\Sigma^-$(0.02)
(6)0$^+$	54608.58	0.38012	336.256	20.2064	1.19374	7.77952	0.2170	$3^3\Sigma^-$(98.55), $3^3\Pi$(1.32), $2^1\Sigma^+$(0.06), $2^3\Pi$(0.04), $3^1\Sigma^+$(0.03)
(10)1	54629.21	0.37990	337.782	20.1862	1.19513	7.78759	0.2169	$3^3\Sigma^-$(99.06), $3^3\Pi$(0.85), $3^1\Pi$(0.04), $2^3\Pi$(0.03), $1^3\Sigma^+$(0.02)
$2^1\Delta_2$	63566.22	0.37395	347.051	2.56385	1.23417	7.29528	0.1664	$2^1\Delta$(99.84), $3^3\Pi$(0.16)
$3^1\Pi_1$	65159.82	0.42902	131.204	33.7622	0.93415	19.5788	0.0205	$3^1\Pi$(99.91), $3^3\Pi$(0.05), $3^3\Sigma^-$(0.04)
$3^1\Sigma^+_{0+}$	77932.37	0.40230	182.059	20.4669	1.06637	12.7012	0.0668	$3^1\Sigma^+$(99.93), $3^3\Pi$(0.04), $3^3\Sigma^-$(0.03)

Figure 1 shows that the $X^3\Sigma^-$, $1^3\Sigma^+$, $2^1\Delta$, $3^1\Pi$, and $3^1\Sigma^+$ states do not cross with other electronic states in the bound region. After considering spin-orbit coupling effects,

these five Λ-S states split into seven Ω states ($X^3\Sigma_{0^+}^-$, $X^3\Sigma_1^-$, $1^3\Sigma_1^+$, $1^3\Sigma_{0^-}^+$, $2^1\Delta_2$, $3^1\Sigma_{0^+}^+$, and $3^1\Pi_1$). The spectral constants of these Ω states differ only slightly from the corresponding values of the five Λ-S states (see Tables 2 and 4). For instance, regarding the potential energy at R_e, the $X^3\Sigma_{0^+}^-$ and $X^3\Sigma_1^-$ states are lower than the $X^3\Sigma^-$ state by 12.95 cm^{-1} and 2.20 cm^{-1}, respectively. The $1^3\Sigma_1^+$ and $1^3\Sigma_{0^-}^+$ states are higher than the $1^3\Sigma^+$ state by 22.95 cm^{-1} and 24.04 cm^{-1}, respectively. The $2^1\Delta_2$ state is 11.41 cm^{-1} higher than the $2^1\Delta$ state. The $3^1\Sigma_{0^+}^+$ state is 14.92 cm^{-1} higher than the $3^1\Sigma^+$ state, and the $3^1\Pi_1$ state is 8.34 cm^{-1} higher than the $3^1\Pi$ state. For the R_e, ω_e, and D_e values, the differences between $1^3\Sigma_{0^-}^+$ and $1^3\Sigma^+$ are 0.00012 nm, 4.202 cm^{-1}, and 0.0006 eV, respectively. The differences between $1^3\Sigma_1^+$ and $1^3\Sigma^+$ are 0.00015 nm, 9.457 cm^{-1}, and 0.0006 eV, respectively. The differences between $2^1\Delta_2$ and $2^1\Delta$ are 0.00007 nm, 0.241 cm^{-1}, and 0.0004 eV. The values for the $3^1\Sigma_{0^+}^+$ state exceed those of the $3^1\Sigma^+$ state by only 0.00001 nm, 0.022 cm^{-1}, and 0 eV. The differences between $3^1\Pi_1$ and $3^1\Pi$ are 0.00002 nm, 0.147 cm^{-1}, and 0.0001 eV.

Including spin-orbit coupling effects, the other 13 Λ-S states split into 28 Ω states (five $\Omega = 0^-$ states, seven $\Omega = 0^+$ states, nine $\Omega = 1$ states, six $\Omega = 2$ states, and one $\Omega = 3$ state). Figure 1 reveals complex crossings among these 13 Λ-S states. This paper discusses only those crossings that affect the potential energy curves of the Ω states. For example, the $a^1\Delta$ and $1^5\Sigma^-$ states intersect at R = 0.23564 nm. The $b^1\Sigma^+$ state crosses with the $A^3\Pi$ and $2^3\Sigma^-$ states at R = 0.21280 nm and R = 0.24478 nm, respectively. The $A^3\Pi$ state also intersects with the $1^5\Sigma^-$ and $2^3\Sigma^-$ states at R = 0.21043 nm and R = 0.30500 nm, respectively. The $c^1\Pi$ state intersects with the $1^5\Sigma^-$, $2^3\Sigma^-$, and $1^3\Delta$ states at R = 0.19560, 0.25592, and 0.37249 nm, respectively. The $2^3\Pi$ state crosses with the $1^5\Sigma^-$, $2^3\Sigma^-$, $1^3\Delta$, and $1^1\Sigma^-$ states at R = 0.13402, 0.17384, 0.19271, and 0.20010 nm, respectively. The $2^1\Pi$ state intersects with the $2^3\Sigma^-$ and $1^3\Delta$ states at R = 0.16183 nm and R = 0.17751 nm, respectively. The $3^3\Sigma^-$ and $3^3\Pi$ states intersect at R = 0.17495 nm. The $2^1\Sigma^+$ state crosses with the $2^3\Sigma^-$, $3^3\Sigma^-$, and $3^3\Pi$ states at R = 0.14225, 0.21551, and 0.22478 nm, respectively. However, within the 28 Ω states under spin-orbit coupling,

these crossings become avoided crossings between Ω states of the same symmetry (0^- and 0^-, 0^+ and 0^+, 1 and 1, 2 and 2). Consequently, except for the $1^3\Delta_3$, $3^3\Pi_2$, and $3^3\Pi_{0^-}$ states, the shapes of the potential energy curves for the other 25 Ω states [including three repulsive states: $(7)0^+$, (11)1, and $(8)0^+$] differ significantly from those of the corresponding Λ-S states (see Figures 1 and 2). Furthermore, the spectral constants of the 22 bound or weakly bound Ω states change substantially compared to those of the corresponding Λ-S states (see Tables 2 and 4). Detailed analysis reveals that: (1) the primary Λ-S components of the $(1)2^{1st\ well}$ ($\upsilon' = 0$–8) and $(2)0^+$ ($\upsilon' = 0$–5) states are the $a^1\Delta$ and $b^1\Sigma^+$ states, respectively; (2) the primary Λ-S component of the $(2)2^{1st\ well}$ ($\upsilon' = 0$–2), $(2)1^{1st\ well}$ ($\upsilon' = 0$–2), $(3)0^+$ ($\upsilon' = 0$–2), and $(1)0^-$ ($\upsilon' = 0$–2) states is the $A^3\Pi$ state. Similar to the OH^+ ion[38], the $A^3\Pi_\Omega$ of the SH^+ ion is also an inverted state. The A_e values obtained in this study are -210.70 cm^{-1} [$(2)2^{1st\ well} - (2)1^{1st\ well}$] and -222.95 cm^{-1} [$(2)1^{1st\ well} - (3)0^+$] (see Table 4). These values agree well with the measured value (-216.95 cm^{-1}) reported by Rostas et al.[14].

3.3 Transition Properties

As analyzed in Section 3.2, the seven Ω states $X^3\Sigma^-_{0^+}$, $X^3\Sigma^-_1$, $(1)2^{1st\ well}$ ($\upsilon' = 0$–8), $(2)0^+$ ($\upsilon' = 0$–5), $(2)2^{1st\ well}$ ($\upsilon' = 0$–2), $(2)1^{1st\ well}$ ($\upsilon' = 0$–2), and $(3)0^+$ ($\upsilon' = 0$–2) are weakly perturbed by other Ω states. In accordance with electric dipole transition selection rules, 12 pairs of transitions occur among these seven Ω states. Tables 5–16 list some relatively large rovibrational transition data for $(1)2^{1st\ well}$ ($\upsilon' = 0$–8, $J' = 2$, +)–$X^3\Sigma^-_1(\upsilon'', J'' = 1, -)$; $(2)0^+$ ($\upsilon' = 0$–5, $J' = 0$, +)–$X^3\Sigma^-_{0^+}(\upsilon'', J'' = 1, -)$/$X^3\Sigma^-_1(\upsilon'', J'' = 1$, –); $(2)2^{1st\ well}$ ($\upsilon' = 0$–2, $J' = 2$, +)–$X^3\Sigma^-_1(\upsilon'', J'' = 1, -)$/$(1)2^{1st\ well}$ ($\upsilon'' = 0$–8, $J'' = 2$, –); $(2)1^{1st\ well}$ ($\upsilon' = 0$–2, $J' = 1$, +)–$X^3\Sigma^-_{0^+}(\upsilon'', J'' = 1, -)$/$X^3\Sigma^-_1(\upsilon'', J'' = 1, -)$/$(1)2^{1st\ well}$ ($\upsilon'' = 0$–8, $J'' = 2$, –)/$(2)0^+$ ($\upsilon'' = 0$–5, $J'' = 1$, –); and $(3)0^+$ ($\upsilon' = 0$–2, $J' = 0$, +)–$X^3\Sigma^-_{0^+}(\upsilon'', J'' = 1, -)$/$X^3\Sigma^-_1(\upsilon'', J'' = 1, -)$/$(2)0^+$ ($\upsilon'' = 0$–5, $J'' = 1$, –). Table 17 presents the $\tau_{\upsilon'J'}$ and Γ_r for the $(1)2^{1st\ well}$ ($\upsilon' = 0$–8, $J' = 2$, +), $(2)0^+$($\upsilon' = 0$–5, $J' = 0$, +), $(2)2^{1st\ well}$ ($\upsilon' = 0$–2, $J' = 2$, +), $(2)1^{1st\ well}$ ($\upsilon' = 0$–2, $J' = 1$, +), and $(3)0^+$($\upsilon' = 0$–2, $J' = 0$, +) states.

Of the 12 rovibronic transition systems listed in Tables 5–16, only the $(1)2^{1st}$

$^{well}(\upsilon' = 0–8,\ J' = 2,\ +)–X^3\Sigma_1^-(\upsilon'',\ J'' = 1,\ –)$ and $(2)0^+(\upsilon' = 0–5,\ J' = 0,\ +)–X^3\Sigma_{0^+}^-(\upsilon'',\ J'' = 1,\ –)/X^3\Sigma_1^-(\upsilon'',\ J'' = 1,\ –)$ transitions exhibit diagonalized $R_{\upsilon'J'\to\upsilon''J''}$. However, these three transition pairs display low spontaneous emission rates and small $gf_{\upsilon'J'\leftarrow\upsilon''J''}$ values. Furthermore, Table 17 indicates that $\tau_{\upsilon'J'}$ are excessively long. Consequently, none of these 12 transition pairs satisfy the criteria for laser cooling of the SH^+ ions.

Table 5 shows that for the $(1)2^{1st\ well}(\upsilon' = 0–8,\ J' = 2,\ +)–X^3\Sigma_1^-(\upsilon'',\ J'' = 1,\ –)$ transition, the $A_{\upsilon'J'\to\upsilon''J''}$, $R_{\upsilon'J'\to\upsilon''J''}$, $gf_{\upsilon'J'\leftarrow\upsilon''J''}$, and $\lambda_{\upsilon'J'\to\upsilon''J''}$ values for the nine faint $\Delta\upsilon = 0$ rovibronic transition lines decrease monotonically as υ' increases. All nine weak spectral lines fall within the near-infrared wavelength range. The corresponding $gf_{\upsilon'J'\leftarrow\upsilon''J''}$ and $\lambda_{\upsilon'J'\to\upsilon''J''}$ ranges are 3.603×10^{-8}–5.323×10^{-8} and 1022.18–1057.35 nm, respectively.

Tables 6 and 7 indicate that two transition systems originating from state $(2)0^+(\upsilon' = 0–5,\ J' = 0,\ +)$ to $X^3\Sigma_{0^+}^-(\upsilon'',\ J'' = 1,\ –)$ and $X^3\Sigma_1^-(\upsilon'',\ J'' = 1,\ –)$ each yield six weak rovibronic spectral lines falling within the visible wavelength range. Moreover, the $R_{\upsilon'J'\to\upsilon''J''}$ and $\lambda_{\upsilon'J'\to\upsilon''J''}$ values of these 12 weak spectral lines with $\Delta\upsilon = 0$ also gradually decrease as υ' increases.

Table 5. Some transition data between the $(1)2^{1st\ well}(\upsilon' = 0—8,\ J' = 2,\ +)$ and $X^3\Sigma_1^-$ $(\upsilon'',\ J'' = 1,\ –)$ states of SH^+ ion.

(υ',υ'')	$\tilde{\upsilon}$/cm^{-1}	$A_{\upsilon'J'\to\upsilon''J''}$/s^{-1}	$R_{\upsilon'J'\to\upsilon''J''}$	$gf_{\upsilon'J'\leftarrow\upsilon''J''}$	$\lambda_{\upsilon'J'\to\upsilon''J''}$/nm	(υ',υ'')	$\tilde{\upsilon}$/cm^{-1}	$A_{\upsilon'J'\to\upsilon''J''}$/s^{-1}	$R_{\upsilon'J'\to\upsilon''J''}$	$gf_{\upsilon'J'\leftarrow\upsilon''J''}$	$\lambda_{\upsilon'J'\to\upsilon''J''}$/nm
(0, 0)	9457.82	0.6352	0.9990	5.323×10^{-8}	1057.35	(1, 1)	9473.61	0.6130	0.9943	5.120×10^{-8}	1055.58
(2, 2)	9494.83	0.5963	0.9900	4.958×10^{-8}	1053.22	(3, 3)	9517.20	0.5831	0.9868	4.825×10^{-8}	1050.75
(4, 4)	9544.13	0.5699	0.9834	4.690×10^{-8}	1047.78	(5, 5)	9577.10	0.5537	0.9786	4.525×10^{-8}	1044.18
(6, 6)	9628.56	0.5322	0.9696	4.303×10^{-8}	1038.60	(7, 7)	9707.30	0.5020	0.9537	3.993×10^{-8}	1030.17
(8, 8)	9783.17	0.4601	0.9383	3.603×10^{-8}	1022.18						

Table 6. Some transition data between the $(2)0^+(\upsilon' = 0—5,\ J' = 0,\ +)$ and $X^3\Sigma_{0^+}^-$ $(\upsilon'',\ J'' = 1,\ –)$ states of SH^+ ion.

(υ',υ'')	$\tilde{\upsilon}$/cm^{-1}	$A_{\upsilon'J'\to\upsilon''J''}$/s^{-1}	$R_{\upsilon'J'\to\upsilon''J''}$	$gf_{\upsilon'J'\leftarrow\upsilon''J''}$	$\lambda_{\upsilon'J'\to\upsilon''J''}$/nm	(υ',υ'')	$\tilde{\upsilon}$/cm^{-1}	$A_{\upsilon'J'\to\upsilon''J''}$/s^{-1}	$R_{\upsilon'J'\to\upsilon''J''}$	$gf_{\upsilon'J'\leftarrow\upsilon''J''}$	$\lambda_{\upsilon'J'\to\upsilon''J''}$/nm
(0, 0)	18300.93	3.7548	0.9954	1.681×10^{-8}	546.43	(1, 1)	18322.48	3.4611	0.9813	1.546×10^{-8}	545.79
(2, 2)	18349.12	2.9931	0.9703	1.333×10^{-8}	545.00	(3, 3)	18391.11	2.4312	0.9460	1.078×10^{-8}	543.75
(4, 4)	18471.66	2.0991	0.9116	9.223×10^{-9}	541.38	(5, 5)	18563.35	2.1080	0.9242	9.171×10^{-9}	538.71

Table 7. Some transition data between the $(2)0^+(\upsilon' = 0—5,\ J' = 0,\ +)$ and $X^3\Sigma_1^-$ $(\upsilon'',\ J'' = 1,\ –)$ states of SH^+ ion.

(υ',υ'')	$\tilde{\upsilon}$/cm^{-1}	$A_{\upsilon'J'\to\upsilon''J''}$/s^{-1}	$R_{\upsilon'J'\to\upsilon''J''}$	$gf_{\upsilon'J'\leftarrow\upsilon''J''}$	$\lambda_{\upsilon'J'\to\upsilon''J''}$/nm	(υ',υ'')	$\tilde{\upsilon}$/cm^{-1}	$A_{\upsilon'J'\to\upsilon''J''}$/s^{-1}	$R_{\upsilon'J'\to\upsilon''J''}$	$gf_{\upsilon'J'\leftarrow\upsilon''J''}$	$\lambda_{\upsilon'J'\to\upsilon''J''}$/nm
(0, 0)	18299.42	1.709×10^2	0.9958	7.653×10^{-7}	546.48	(1, 1)	18320.74	1.655×10^2	0.9864	7.393×10^{-7}	545.84
(2, 2)	18347.15	1.624×10^2	0.9801	7.234×10^{-7}	545.05	(3, 3)	18388.92	1.631×10^2	0.9768	7.232×10^{-7}	543.82
(4, 4)	18469.26	1.701×10^2	0.9762	7.474×10^{-7}	541.45	(5, 5)	18560.75	1.841×10^2	0.9747	8.011×10^{-7}	538.78

Table 8 indicates that the 11 strong rovibronic emission lines of the (2)$2^{1st\ well}$(υ' = 0–2, J' = 2, +)–$X^3\Sigma_1^-$(υ'', J'' = 1, –) system are concentrated in the near-ultraviolet to violet region (304.34–424.17 nm). For a fixed υ', $\lambda_{\upsilon'J'\rightarrow\upsilon''J''}$ increases gradually with rising υ'', whereas $\tilde{\upsilon}$ decreases. The $\tilde{\upsilon}$ value for the (0, 0) band obtained in this study is 68.66 cm^{-1} (0.231%) higher than the experimental value reported by Rostas et al.[14]. Furthermore, the calculated $\tilde{\upsilon}$ values for the (0, 0), (0, 1), and (0, 2) bands of the (2)$2^{1st\ well}$(υ' = 0–2, J' = 4, +)–$X^3\Sigma_1^-$(υ'', J'' = 4, –) system are 29731.43, 27270.92, and 24907.63 cm^{-1}, respectively. The deviations from the corresponding experimental values of Rostas et al.[14] are only 18.89 cm^{-1} (0.064%), 4.21 cm^{-1} (0.015%), and 12.60 cm^{-1} (0.051%), respectively. The $\tilde{\upsilon}$ value (24168.67 cm^{-1}) for the (2)$2^{1st\ well}$(υ' = 1, J' = 3, +)–$X^3\Sigma_1^-$(υ'' = 3, J'' = 4, –) transition is 16.87 cm^{-1} (0.070%) lower than the experimental value (24185.54 cm^{-1}) reported by Edwards et al.[16]. Table 9 shows that the wavelengths of the 17 weak rovibronic emission lines for the (2)$2^{1st\ well}$(υ' = 0–2, J' = 2, +)–(1)$2^{1st\ well}$(υ'' = 0–8, J'' = 2, –) transition cover the visible to near-infrared region (455.94–1261.63 nm). The corresponding $gf_{\upsilon'J'\leftarrow\upsilon''J''}$ values range from 9.610×10^{-8} to 2.666×10^{-6}. In summary, the (2)$2^{1st\ well}$(υ' = 0–2, J' = 2, +)–$X^3\Sigma_1^-$(υ'', J'' = 1, –) transition is the primary factor determining the $\tau_{\upsilon'J'}$ of the (2)$2^{1st\ well}$(υ' = 0–2, J' = 2, +) state.

Table 8. Some transition data between the (2)$2^{1st\ well}$(υ' = 0—2, J' = 2, +) and $X^3\Sigma_1^-$ (υ'', J'' = 1, –) states of SH^+ ion.

(υ', υ'')	$\tilde{\upsilon}$/cm^{-1}	$A_{\upsilon'J'\rightarrow\upsilon''J''}$/$s^{-1}$	$R_{\upsilon'J'\rightarrow\upsilon''J''}$	$gf_{\upsilon'J'\leftarrow\upsilon''J''}$	$\lambda_{\upsilon'J'\rightarrow\upsilon''J''}$/nm	(υ', υ'')	$\tilde{\upsilon}$/cm^{-1}	$A_{\upsilon'J'\rightarrow\upsilon''J''}$/$s^{-1}$	$R_{\upsilon'J'\rightarrow\upsilon''J''}$	$gf_{\upsilon'J'\leftarrow\upsilon''J''}$	$\lambda_{\upsilon'J'\rightarrow\upsilon''J''}$/nm
(0, 0)	29791.13	5.022×10^{5}	0.7616	4.241×10^{-8}	335.68	(0, 1)	27325.55	1.384×10^{5}	0.2099	1.389×10^{-8}	365.97
(0, 2)	24957.19	1.752×10^{4}	0.0266	2.109×10^{-4}	400.69	(1, 0)	31381.91	4.461×10^{5}	0.7076	3.395×10^{-8}	318.66
(1, 1)	28916.33	4.598×10^{4}	0.0730	4.122×10^{-4}	345.83	(1, 2)	26547.98	1.048×10^{5}	0.1662	1.114×10^{-8}	376.68
(1, 3)	24275.34	2.993×10^{4}	0.0475	3.807×10^{-4}	411.95	(2, 0)	32859.06	2.367×10^{5}	0.4122	1.643×10^{-8}	304.34
(2, 1)	30393.48	2.605×10^{5}	0.4536	2.114×10^{-8}	329.02	(2, 3)	25752.49	3.552×10^{4}	0.0619	4.014×10^{-4}	388.32
(2, 4)	23575.92	2.746×10^{4}	0.0478	3.703×10^{-4}	424.17						

Table 9. Some transition data between the $(2)2^{1st\ well}(\upsilon' = 0—2,\ J' = 2,\ +)$ and $(1)2^{1st\ well}(\upsilon'' = 0—8,\ J'' = 2,\ -)$ states of SH^+ ion.

$(\upsilon',\ \upsilon'')$	$\tilde{\upsilon}$/cm^{-1}	$A_{\upsilon'J'\to\upsilon''J''}$/s^{-1}	$R_{\upsilon'J'\to\upsilon''J''}$	$gf_{\upsilon'J'\leftarrow\upsilon''J''}$	$\lambda_{\upsilon'J'\to\upsilon''J''}$/nm	$(\upsilon',\ \upsilon'')$	$\tilde{\upsilon}$/cm^{-1}	$A_{\upsilon'J'\to\upsilon''J''}$/s^{-1}	$R_{\upsilon'J'\to\upsilon''J''}$	$gf_{\upsilon'J'\leftarrow\upsilon''J''}$	$\lambda_{\upsilon'J'\to\upsilon''J''}$/nm
(0, 0)	20342.46	56.837	0.3254	1.030×10^{-6}	491.59	(0, 1)	17860.81	79.289	0.4540	1.863×10^{-6}	559.90
(0, 2)	15470.96	33.604	0.1924	1.052×10^{-6}	646.39	(0, 3)	13175.67	4.563	0.0261	1.970×10^{-7}	758.99
(1, 0)	21933.18	9.742	0.0561	1.518×10^{-7}	455.94	(1, 1)	19451.53	8.828	0.0508	1.749×10^{-7}	514.11
(1, 2)	17061.67	71.270	0.4104	1.835×10^{-6}	586.12	(1, 3)	14766.38	63.508	0.3657	2.183×10^{-6}	677.23
(1, 4)	12562.64	17.867	0.1029	8.486×10^{-7}	796.03	(1, 5)	10448.91	2.148	0.0124	1.474×10^{-7}	957.06
(2, 1)	20927.61	23.542	0.1347	4.029×10^{-7}	477.85	(2, 2)	18537.75	4.406	0.0252	9.610×10^{-8}	539.45
(2, 3)	16242.46	29.571	0.1691	8.402×10^{-7}	615.68	(2, 4)	14038.72	70.094	0.4009	2.666×10^{-6}	712.33
(2, 5)	11924.99	36.150	0.2068	1.906×10^{-6}	838.59	(2, 6)	9889.51	8.857	0.0507	6.788×10^{-7}	1011.19
(2, 7)	7926.40	1.782	0.0102	2.126×10^{-7}	1261.63						

Table 10 indicates that the 12 strong rovibronic emission lines of the $(2)1^{1st\ well}(\upsilon' = 0–2,\ J' = 1,\ +)–X^3\Sigma_{0^+}^-(\upsilon'',\ J'' = 1,\ -)$ system cover the spectral range from near-ultraviolet to violet (302.44–420.49 nm). The corresponding $gf_{\upsilon'J'\leftarrow\upsilon''J''}$ values range from 7.791×10^{-5} to 4.269×10^{-3}. Furthermore, the *Q*-branch $\tilde{\upsilon}$ values for the $(2)1^{1st\ well}(\upsilon' = 1,\ J' = 1–3,\ +)–X^3\Sigma_{0^+}^-(\upsilon'' = 0,\ J'' = 1–3,\ -)$ system obtained in this study are 31594.50, 31586.43, and 31574.32 cm^{-1}, respectively. These values are higher than the experimental results reported by Edwards et al.[16] by 86.89 cm^{-1} (0.276%), 76.16 cm^{-1} (0.242%), and 69.84 cm^{-1} (0.222%), respectively. In contrast, the *R*-branch $\tilde{\upsilon}$ values (24539.98 and 24539.74 cm^{-1}) for the $(2)1^{1st\ well}(\upsilon' = 1,\ J' = 6$ and 7, $+)–X^3\Sigma_{0^+}^-(\upsilon'' = 3,\ J'' = 5$ and 6, $-)$ system are lower than the experimental values of Edwards et al.[16] by 31.70 cm^{-1} (0.129%) and 48.33 cm^{-1} (0.197%), respectively. Table 11 shows that the 19 weak rovibronic emission lines of the $(2)1^{1st\ well}(\upsilon' = 0–2,\ J' = 1,\ +)–X^3\Sigma_1^-(\upsilon'',\ J'' = 1,\ -)$ system, ranging from near-ultraviolet to red light, are distributed within the wavelength range of 302.45–623.63 nm. The corresponding $gf_{\upsilon'J'\leftarrow\upsilon''J''}$ values range from 5.091×10^{-9} to 7.123×10^{-7}. According to Table 12, the $(2)1^{1st\ well}(\upsilon' = 0–2,\ J' = 1,\ +)–(1)2^{1st\ well}(\upsilon'' = 0–8,\ J'' = 2,\ -)$ system yields 12 weak rovibronic emission lines in the visible region. The corresponding $\lambda_{\upsilon'J'\to\upsilon''J''}$ ranges from 423.65 to 702.53 nm, and the $gf_{\upsilon'J'\leftarrow\upsilon''J''}$ ranges from 2.806×10^{-8} to 9.477×10^{-7}. Table 13 indicates that the $(2)1^{1st\ well}(\upsilon' = 0–2,\ J' = 1,\ +)–(2)0^+(\upsilon'' = 0–5,\ J'' = 1,\ -)$ transition produces six weak rovibronic emission lines spanning the red to near-infrared region (675.08–1188.64

nm). The corresponding $gf_{\upsilon' J' \leftarrow \upsilon'' J''}$ values range from 8.569×10^{-8} to 3.328×10^{-7}. Therefore, the $(2)1^{1\text{st well}}(\upsilon' = 0\text{–}2, J' = 1, +)\text{–}X^3\Sigma_{0^+}^-(\upsilon'', J'' = 1, -)$ transition is the primary factor determining the $\tau_{\upsilon' J'}$ of the $(2)1^{1\text{st well}}(\upsilon' = 0\text{–}2, J' = 1, +)$ state.

Table 10. Some transition data between the $(2)1^{1\text{st well}}$ ($\upsilon' = 0$—2, $J' = 1, +$) and $X^3\Sigma_{0^+}^-$ ($\upsilon'', J'' = 1, -$) states of SH^+ ion.

(υ', υ'')	$\tilde{\upsilon}$/cm^{-1}	$A_{\upsilon' J' \to \upsilon'' J''}$/s^{-1}	$R_{\upsilon' J' \to \upsilon'' J''}$	$gf_{\upsilon' J' \leftarrow \upsilon'' J''}$	$\lambda_{\upsilon' J' \to \upsilon'' J''}$/nm	(υ', υ'')	$\tilde{\upsilon}$/cm^{-1}	$A_{\upsilon' J' \to \upsilon'' J''}$/s^{-1}	$R_{\upsilon' J' \to \upsilon'' J''}$	$gf_{\upsilon' J' \leftarrow \upsilon'' J''}$	$\lambda_{\upsilon' J' \to \upsilon'' J''}$/nm
(0, 0)	30004.43	8.544×10^{5}	0.7611	4.269×10^{-8}	333.29	(0, 1)	27538.80	2.360×10^{5}	0.2102	1.400×10^{-8}	363.13
(0, 2)	25170.39	2.998×10^{4}	0.0267	2.129×10^{-4}	397.30	(1, 0)	31594.50	7.584×10^{5}	0.7072	3.417×10^{-8}	316.52
(1, 1)	29128.88	7.803×10^{4}	0.0728	4.136×10^{-4}	343.31	(1, 2)	26760.47	1.786×10^{5}	0.1665	1.122×10^{-8}	373.69
(1, 3)	24487.76	5.120×10^{4}	0.0477	3.840×10^{-4}	408.38	(2, 0)	33065.48	3.964×10^{5}	0.4128	1.631×10^{-8}	302.44
(2, 1)	30599.85	4.342×10^{5}	0.4521	2.085×10^{-8}	326.81	(2, 2)	28231.44	1.381×10^{4}	0.0144	7.791×10^{-5}	354.22
(2, 3)	25958.74	5.886×10^{4}	0.0613	3.928×10^{-4}	385.23	(2, 4)	23782.10	4.634×10^{4}	0.0483	3.685×10^{-4}	420.49

Table 11. Some transition data between the $(2)1^{1\text{st well}}(\upsilon' = 0$—$2, J' = 1, +)$ and $X^3\Sigma_1^-$ ($\upsilon'', J'' = 1, -$) states of SH^+ ion.

(υ', υ'')	$\tilde{\upsilon}$/cm^{-1}	$A_{\upsilon' J' \to \upsilon'' J''}$/s^{-1}	$R_{\upsilon' J' \to \upsilon'' J''}$	$gf_{\upsilon' J' \leftarrow \upsilon'' J''}$	$\lambda_{\upsilon' J' \to \upsilon'' J''}$/nm	(υ', υ'')	$\tilde{\upsilon}$/cm^{-1}	$A_{\upsilon' J' \to \upsilon'' J''}$/s^{-1}	$R_{\upsilon' J' \to \upsilon'' J''}$	$gf_{\upsilon' J' \leftarrow \upsilon'' J''}$	$\lambda_{\upsilon' J' \to \upsilon'' J''}$/nm
(0, 0)	30002.92	62.872	0.3531	3.141×10^{-7}	333.31	(0, 1)	27537.06	76.527	0.4298	4.539×10^{-7}	363.15
(0, 2)	25168.43	31.614	0.1775	2.245×10^{-7}	397.33	(0, 3)	22895.51	6.318	0.0355	5.421×10^{-8}	436.78
(1, 0)	31593.00	16.355	0.0797	7.370×10^{-8}	316.53	(1, 1)	29127.13	8.333	0.0406	4.418×10^{-8}	343.33
(1, 2)	26758.50	80.778	0.3937	5.074×10^{-7}	373.72	(1, 3)	24485.58	70.939	0.3458	5.322×10^{-7}	408.41
(1, 4)	22308.73	23.836	0.1162	2.154×10^{-7}	448.26	(1, 5)	20227.66	4.288	0.0209	4.714×10^{-8}	494.38
(2, 0)	33063.97	1.237	0.0052	5.091×10^{-9}	302.45	(2, 1)	30598.11	20.696	0.0873	9.942×10^{-8}	326.82
(2, 2)	28229.47	4.419	0.0186	2.494×10^{-8}	354.25	(2, 3)	25956.56	36.607	0.1544	2.444×10^{-7}	385.27
(2, 4)	23779.70	89.554	0.3777	7.123×10^{-7}	420.54	(2, 5)	21698.64	56.319	0.2375	5.380×10^{-7}	460.87
(2, 6)	19713.06	19.252	0.0812	2.228×10^{-7}	507.29	(2, 7)	17824.76	5.842	0.0246	8.270×10^{-8}	561.03
(2, 8)	16035.54	2.079	0.0088	3.636×10^{-8}	623.63						

Table 12. Some transition data between the $(2)1^{1\text{st well}}(\upsilon' = 0$—$2, J' = 1, +)$ and $(1)2^{1\text{st well}}(\upsilon'' = 0$—$8, J'' = 2, -)$ states of SH^+ ion.

(υ', υ'')	$\tilde{\upsilon}$/cm^{-1}	$A_{\upsilon' J' \to \upsilon'' J''}$/s^{-1}	$R_{\upsilon' J' \to \upsilon'' J''}$	$gf_{\upsilon' J' \leftarrow \upsilon'' J''}$	$\lambda_{\upsilon' J' \to \upsilon'' J''}$/nm	(υ', υ'')	$\tilde{\upsilon}$/cm^{-1}	$A_{\upsilon' J' \to \upsilon'' J''}$/s^{-1}	$R_{\upsilon' J' \to \upsilon'' J''}$	$gf_{\upsilon' J' \leftarrow \upsilon'' J''}$	$\lambda_{\upsilon' J' \to \upsilon'' J''}$/nm
(0, 0)	20545.10	88.944	0.7458	9.477×10^{-7}	486.74	(0, 1)	18063.45	26.534	0.2225	3.658×10^{-7}	553.62
(0, 2)	15673.59	3.527	0.0296	6.457×10^{-7}	638.03	(1, 0)	22135.10	78.468	0.7088	7.203×10^{-7}	451.78
(1, 1)	19653.45	6.985	0.0631	8.134×10^{-8}	508.83	(1, 2)	17263.59	18.942	0.1711	2.858×10^{-7}	579.27
(1, 3)	14968.31	5.666	0.0512	1.137×10^{-7}	668.09	(2, 0)	23605.03	40.211	0.4137	3.246×10^{-7}	423.65
(2, 1)	21123.38	43.820	0.4508	4.417×10^{-7}	473.42	(2, 2)	18733.53	2.190	0.0225	2.806×10^{-8}	533.81
(2, 3)	16438.24	5.374	0.0553	8.945×10^{-8}	608.35	(2, 4)	14234.49	4.619	0.0475	1.025×10^{-7}	702.53

Table 14 indicates that the $(3)0^+(\upsilon' = 0\text{–}2, J' = 0, +)\text{–}X^3\Sigma_1^-(\upsilon'', J'' = 1, -)$ transition yields 11 strong emission lines distributed across the near-ultraviolet to violet region (299.77–415.38 nm). The corresponding $gf_{\upsilon' J' \leftarrow \upsilon'' J''}$ values range from 7.082×10^{-5} to 1.442×10^{-3}. Table 15 shows that the $(3)0^+(\upsilon' = 0\text{–}2, J' = 0, +)\text{–}X^3\Sigma_{0^+}^-(\upsilon'', J'' = 1, -)$ transition produces 16 weak emission lines extending from the near-ultraviolet to the green region (314.12–551.80 nm). The associated $gf_{\upsilon' J' \leftarrow \upsilon'' J''}$ values range from

5.232×10^{-8} to 9.560×10^{-7}. According to Table 16, the $(3)0^{+}(\upsilon' = 0\text{–}2, J' = 0, +)$–$(2)0^{+}(\upsilon'' = 0\text{–}5, J'' = 1, -)$ transition yields 13 weak emission lines spanning from the red to the near-infrared region (665.45–2919.77 nm). The corresponding $gf_{\upsilon' J' \leftarrow \upsilon'' J''}$ values range from 1.195×10^{-8} to 6.797×10^{-7}. Consequently, the $(3)0^{+}(\upsilon' = 0\text{–}2, J' = 0, +)$–$X^3\Sigma_1^-(\upsilon'', J'' = 1, -)$ transition is the primary contributor to the $\tau_{\upsilon' J'}$ of the $(3)0^{+}(\upsilon' = 0\text{–}2, J' = 0, +)$ state. Furthermore, for a constant υ', the $\lambda_{\upsilon' J' \rightarrow \upsilon'' J''}$ values for these nine transition pairs from the $(2)2^{1\text{st well}}(\upsilon' = 0\text{–}2, J' = 2, +)$, $(2)1^{1\text{st well}}(\upsilon' = 0\text{–}2, J' = 1, +)$, and $(3)0^{+}(\upsilon' = 0\text{–}2, J' = 0, +)$ states gradually increase with increasing υ''. In contrast, $\tilde{\upsilon}$ gradually decreases as υ'' increases (see Tables 8–16).

Table 13. Some transition data between the $(2)1^{1\text{st well}}(\upsilon' = 0\text{—}2, J' = 1, +)$ and $(2)0^{+}(\upsilon'' = 0\text{—}5, J'' = 1, -)$ states of SH^+ ion.

(υ', υ'')	$\tilde{\upsilon}$/cm^{-1}	$A_{\upsilon' J' \rightarrow \upsilon'' J''}$/s^{-1}	$R_{\upsilon' J' \rightarrow \upsilon'' J''}$	$gf_{\upsilon' J' \leftarrow \upsilon'' J''}$	$\lambda_{\upsilon' J' \rightarrow \upsilon'' J''}$/nm	(υ', υ'')	$\tilde{\upsilon}$/cm^{-1}	$A_{\upsilon' J' \rightarrow \upsilon'' J''}$/s^{-1}	$R_{\upsilon' J' \rightarrow \upsilon'' J''}$	$gf_{\upsilon' J' \leftarrow \upsilon'' J''}$	$\lambda_{\upsilon' J' \rightarrow \upsilon'' J''}$/nm
(0, 0)	11686.65	10.107	0.8178	3.328×10^{-7}	855.69	(0, 1)	9200.04	2.072	0.1677	1.101×10^{-7}	1086.97
(1, 0)	13293.93	10.976	0.8215	2.793×10^{-7}	752.24	(1, 2)	8413.11	1.349	0.1009	8.569×10^{-8}	1188.64
(2, 0)	14813.38	6.665	0.5044	1.366×10^{-7}	675.08	(2, 1)	12326.78	5.839	0.4419	1.728×10^{-7}	811.26

Table 14. Some transition data between the $(3)0^{+}(\upsilon' = 0\text{—}2, J' = 0, +)$ and $X^3\Sigma_1^-$ $(\upsilon'', J'' = 1, -)$ states of SH^+ ion.

(υ', υ'')	$\tilde{\upsilon}$/cm^{-1}	$A_{\upsilon' J' \rightarrow \upsilon'' J''}$/s^{-1}	$R_{\upsilon' J' \rightarrow \upsilon'' J''}$	$gf_{\upsilon' J' \leftarrow \upsilon'' J''}$	$\lambda_{\upsilon' J' \rightarrow \upsilon'' J''}$/nm	(υ', υ'')	$\tilde{\upsilon}$/cm^{-1}	$A_{\upsilon' J' \rightarrow \upsilon'' J''}$/s^{-1}	$R_{\upsilon' J' \rightarrow \upsilon'' J''}$	$gf_{\upsilon' J' \leftarrow \upsilon'' J''}$	$\lambda_{\upsilon' J' \rightarrow \upsilon'' J''}$/nm
(0, 0)	30220.38	8.784×10^{5}	0.7618	1.442×10^{-3}	330.91	(0, 1)	27754.52	2.421×10^{5}	0.2100	4.711×10^{-4}	360.31
(0, 2)	25385.89	3.044×10^{4}	0.0264	7.082×10^{-5}	393.93	(1, 0)	31833.68	7.924×10^{5}	0.7038	1.172×10^{-3}	314.14
(1, 1)	29367.82	8.847×10^{4}	0.0786	1.538×10^{-4}	340.52	(1, 2)	26999.18	1.889×10^{5}	0.1678	3.885×10^{-4}	370.39
(1, 3)	24726.26	5.087×10^{4}	0.0452	1.247×10^{-4}	404.44	(2, 0)	33359.17	4.025×10^{5}	0.3968	5.423×10^{-4}	299.77
(2, 1)	30893.31	4.746×10^{5}	0.4679	7.455×10^{-4}	323.71	(2, 3)	26251.75	7.124×10^{4}	0.0702	1.550×10^{-4}	380.93
(2, 4)	24074.90	4.774×10^{4}	0.0471	1.235×10^{-4}	415.38						

Table 15. Some transition data between the $(3)0^{+}(\upsilon' = 0\text{–}2, J' = 0, +)$ and $X^3\Sigma_{0+}^-$ $(\upsilon'', J'' = 1, -)$ states of SH^+ ion.

(υ', υ'')	$\tilde{\upsilon}$/cm^{-1}	$A_{\upsilon' J' \rightarrow \upsilon'' J''}$/s^{-1}	$R_{\upsilon' J' \rightarrow \upsilon'' J''}$	$gf_{\upsilon' J' \leftarrow \upsilon'' J''}$	$\lambda_{\upsilon' J' \rightarrow \upsilon'' J''}$/nm	(υ', υ'')	$\tilde{\upsilon}$/cm^{-1}	$A_{\upsilon' J' \rightarrow \upsilon'' J''}$/s^{-1}	$R_{\upsilon' J' \rightarrow \upsilon'' J''}$	$gf_{\upsilon' J' \leftarrow \upsilon'' J''}$	$\lambda_{\upsilon' J' \rightarrow \upsilon'' J''}$/nm
(0, 0)	30221.89	2.335×10^{2}	0.3515	3.832×10^{-7}	330.89	(0, 1)	27756.27	2.860×10^{2}	0.4306	5.565×10^{-7}	360.29
(0, 2)	25387.85	1.185×10^{2}	0.1783	2.755×10^{-7}	393.90	(0, 3)	23115.15	23.586	0.0355	6.618×10^{-8}	432.63
(1, 0)	31835.19	59.208	0.0760	8.758×10^{-8}	314.12	(1, 1)	29369.57	34.969	0.0449	6.078×10^{-8}	340.50
(1, 2)	27001.15	3.141×10^{2}	0.4033	6.458×10^{-7}	370.36	(1, 3)	24728.45	2.677×10^{2}	0.3438	6.563×10^{-7}	404.40
(1, 4)	22551.81	86.173	0.1107	2.540×10^{-7}	443.43	(1, 5)	20470.94	14.625	0.0188	5.232×10^{-8}	488.51
(2, 1)	30895.06	76.543	0.0812	1.202×10^{-7}	323.68	(2, 3)	26253.94	1.715×10^{2}	0.1820	3.730×10^{-7}	380.90
(2, 4)	24077.30	3.697×10^{2}	0.3924	9.560×10^{-7}	415.34	(2, 5)	21996.43	2.178×10^{2}	0.2312	6.749×10^{-7}	454.63
(2, 6)	20011.00	69.369	0.0736	2.597×10^{-7}	499.74	(2, 7)	18122.83	17.788	0.0189	8.119×10^{-8}	551.80

Table 16. Some transition data between the $(3)0^{+}(\upsilon' = 0\text{–}2, J' = 0, +)$ and $(2)0^{+}(\upsilon'' = 0\text{–}5, J'' = 1, -)$ states of SH^+ ion.

(υ', υ'')	$\tilde{\upsilon}$/cm^{-1}	$A_{\upsilon' J' \rightarrow \upsilon'' J''}$/s^{-1}	$R_{\upsilon' J' \rightarrow \upsilon'' J''}$	$gf_{\upsilon' J' \leftarrow \upsilon'' J''}$	$\lambda_{\upsilon' J' \rightarrow \upsilon'' J''}$/nm	(υ', υ'')	$\tilde{\upsilon}$/cm^{-1}	$A_{\upsilon' J' \rightarrow \upsilon'' J''}$/s^{-1}	$R_{\upsilon' J' \rightarrow \upsilon'' J''}$	$gf_{\upsilon' J' \leftarrow \upsilon'' J''}$	$\lambda_{\upsilon' J' \rightarrow \upsilon'' J''}$/nm
(0, 0)	11902.04	34.195	0.5205	3.619×10^{-7}	840.21	(0, 1)	9415.43	25.044	0.3812	4.235×10^{-7}	1062.11
(0, 2)	7021.23	5.868	0.0893	1.785×10^{-7}	1424.28	(1, 0)	13509.02	12.903	0.2396	1.060×10^{-7}	740.26
(1, 1)	11022.41	4.141	0.0769	5.110×10^{-8}	907.26	(1, 2)	8628.21	23.338	0.4333	4.700×10^{-7}	1159.01
(1, 3)	6316.42	11.530	0.2141	4.333×10^{-7}	1583.21	(1, 4)	4068.11	1.859	0.0345	1.684×10^{-7}	2458.19
(2, 0)	15027.62	1.800	0.0396	1.195×10^{-8}	665.45	(2, 1)	12541.01	12.873	0.2830	1.227×10^{-7}	797.40
(2, 3)	7835.03	11.554	0.2540	2.822×10^{-7}	1276.34	(2, 4)	5586.71	14.151	0.3111	6.797×10^{-7}	1790.00
(2, 5)	3424.99	3.968	0.0872	5.072×10^{-7}	2919.77						

Table 17. The $\tau_{\upsilon'J'}$ and Γ_r of (1)$2^{1st\ well}$(υ' = 0–8, J' = 2, +), (2)0^+(υ' = 0–5, J' = 0, +), (2)$2^{1st\ well}$(υ' = 0–2, J' = 2, +), (2)$1^{1st\ well}$ (υ' = 0–2, J' = 1, +) , and (3)0^+(υ' = 0–2, J' = 0, +) states for the SH^+ ion calculated in this study.

	(1)$2^{第一势阱}$(J' = 2, +)		(2)0^+(J' = 0, +)		(2)$2^{第一势阱}$(J' = 2, +)		(2)$1^{第一势阱}$(J' = 1, +)		(3)0^+(J' = 0, +)	
υ'	$\tau_{\upsilon'J'}$/s	Γ_r/cm^{-1}	$\tau_{\upsilon'J'}$/ms	Γ_r/cm^{-1}	$\tau_{\upsilon'J'}$/μs	Γ_r/cm^{-1}	$\tau_{\upsilon'J'}$/ns	Γ_r/cm^{-1}	$\tau_{\upsilon'J'}$/ns	Γ_r/cm^{-1}
0	1.573	3.375×10^{-12}	5.700	9.314×10^{-10}	1.516	3.501×10^{-6}	890.537	5.961×10^{-6}	866.778	6.125×10^{-6}
1	1.622	3.273×10^{-12}	5.836	9.096×10^{-10}	1.586	3.347×10^{-6}	932.228	5.695×10^{-6}	887.603	5.981×10^{-6}
2	1.660	3.198×10^{-12}	5.923	8.962×10^{-10}	1.741	3.049×10^{-6}	1040.960	5.100×10^{-6}	984.951	5.390×10^{-6}
3	1.692	3.137×10^{-12}	5.897	9.002×10^{-10}						
4	1.726	3.077×10^{-12}	5.665	9.371×10^{-10}						
5	1.767	3.004×10^{-12}	5.232	1.015×10^{-9}						
6	1.822	2.914×10^{-12}								
7	1.900	2.794×10^{-12}								
8	2.039	2.603×10^{-12}								

As shown in Table 17, the $\tau_{\upsilon'J'}$ values for the four states (1)$2^{1st\ well}$ (υ' = 0–8, J' = 2, +), (2)$2^{1st\ well}$ (υ' = 0–2, J' = 2, +), (2)$1^{1st\ well}$ (υ' = 0–2, J' = 1, +), and (3)0^+ (υ' = 0–2, J' = 0, +) gradually increase with increasing υ', whereas the Γ_r values gradually decrease. The variations in $\tau_{\upsilon'J'}$ with respect to υ' for these four states do not exceed 0.466 s, 0.225 μs, 150.423 ns, and 118.173 ns, respectively. For the (2)0^+ (υ' = 0–5, J' = 0, +) state, $\tau_{\upsilon'J'}$ initially increases and then decreases as υ' increases, while Γ_r initially decreases and then increases. The variation range of $\tau_{\upsilon'J'}$ for this state does not exceed 0.691 ms.

We briefly investigated the variation of $\tau_{\upsilon'J'}$ with the rotational quantum number J' for the (2)$2^{1st\ well}$ (υ' = 0–2, +), (2)$1^{1st\ well}$ (υ' = 0–2, +), and (3)0^+ (υ' = 0–2, +) states (see Figures 4–6). Similar to the $A^1\Pi_1$ (υ' = 0 and 1, +) state of the AlH molecule [37] and the (2)$2^{1st\ well}$ (υ' = 0–2, +), (2)1 (υ' = 0–9, +), and (1)0^- (υ' = 0–8, +) states of the OH^+ ion [38], the $\tau_{\upsilon'J'}$ values for these three states of the SH^+ ion also gradually increase with increasing J'. For the (2)$2^{1st\ well}$ (υ' = 0–2, +) state, the variations in $\tau_{\upsilon'J'}$ with J' are less than 11.48, 5.93, and 3.91 μs when υ' = 0 with $J' \leq 38$, υ' = 1 with $J' \leq 29$, and υ' = 2 with $J' \leq 18$, respectively (see Figure 4). For the (2)$1^{1st\ well}$ (υ' = 0–2, +) state, the variations in $\tau_{\upsilon'J'}$ with J' are less than 2.85, 1.02, and 0.47 μs when υ' = 0 with $J' \leq 39$, υ' = 1 with $J' \leq 28$, and υ' = 2 with $J' \leq 16$, respectively (see Figure 5). For the (3)0^+ (υ' = 0–2, +) state, the variations in $\tau_{\upsilon'J'}$ with J' do not exceed 13.02, 7.18, and 5.51 μs when υ' = 0 with $J' \leq 39$, υ' = 1 with $J' \leq 29$, and υ' = 2 with $J' \leq 18$, respectively (see Figure 6). All datasets

from this study are provided in xls format in the supplementary materials. These include the potential energy curves for 18 Λ-S states and 35 Ω states; the 12 pairs of transition dipole moments among seven Ω states [$X^3\Sigma_{0^+}^-$, $X^3\Sigma_1^-$, (1)$2^{1st\ well}$ (υ' = 0–8), (2)0^+ (υ' = 0–5), (2)$2^{1st\ well}$ (υ' = 0–2), (2)$1^{1st\ well}$ (υ' = 0–2), and (3)0^+ (υ' = 0–2)]; and the variation of $\tau_{\upsilon'J'}$ with J' for the (2)$2^{1st\ well}$ (υ' = 0–2, +), (2)$1^{1st\ well}$ (υ' = 0–2, +), and (3)0^+ (υ' = 0–2, +) states.

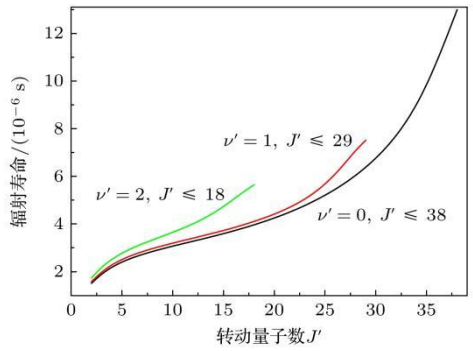

Fig. 4 Variation of $\tau_{\upsilon'J'}$ with J' for the (2)$2^{1st\ well}$ (υ' = 0–2, +) state of the SH^+ ion.

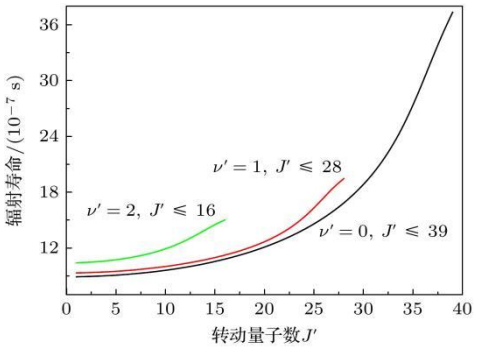

Fig. 5 Variation of $\tau_{\upsilon'J'}$ with J' for the (2)$1^{1st\ well}$ (υ' = 0–2, +) state of the SH^+ ion.

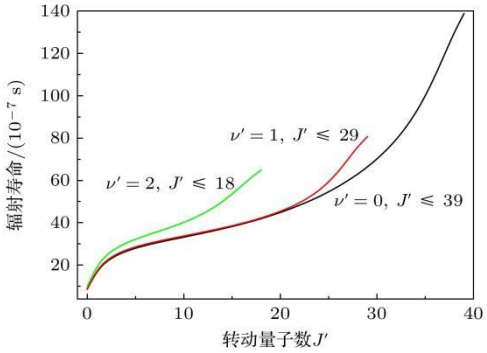

Fig. 6 Variation of $\tau_{\upsilon'J'}$ with J' for the (3)0^+(υ' = 0–2, +) state of the SH^+ ion.

4 Conclusions

This study investigated the spectroscopic and transition properties of 18 Λ-S states and 35 Ω states of the SH^+ ion. We systematically considered various physical effects, including core-valence electron correlation, scalar relativistic effects, spin-orbit coupling, and the complete basis set limit. The calculations employed the optimized icMRCI+*Q* method combined with quantum mechanical approaches. The computed spectroscopic constants, molecular constants, and rovibrational transition data agree well with experimental measurements. These results provide data support for subsequent experimental studies and astronomical observations. The findings are as follows: 1) For a fixed υ', the $\tau_{\upsilon'J'}$ values of five excited Ω states [(1)$2^{1st\ well}$(J' = 2, +), (2)0^+(J' = 0, +), (2)$2^{1st\ well}$(J' = 2, +), (2)$1^{1st\ well}$(J' = 1, +), and (3)0^+(J' = 0, +)] decrease sequentially, while the Γ_r values increase sequentially. Furthermore, for the (1)$2^{1st\ well}$(υ' = 0–8, J' = 2, +), (2)$2^{1st\ well}$(υ' = 0–2, J' = 2, +), (2)$1^{1st\ well}$(υ' = 0–2, J' = 1, +), and (3)0^+(υ' = 0–2, J' = 0, +) states, the $\tau_{\upsilon'J'}$ values gradually increases with increasing υ', whereas Γ_r gradually decreases. For the (2)0^+(υ' = 0–5, J' = 0, +) state, $\tau_{\upsilon'J'}$ first increases and then decreases as υ' increases, while Γ_r first decreases and then increases. 2) The spontaneous radiation is strong for three systems: (2)$2^{1st\ well}$(υ' = 0–2, J' = 2, +)/(3)0^+(υ' = 0–2, J' = 0, +)–$X^3\Sigma_1^-$(υ'', J''= 1, –) and (2)$1^{1st\ well}$(υ' = 0–2, J' = 1, +)–$X^3\Sigma_{0^+}^-$(υ'', J'' = 1, –). The strong radiation is concentrated in the near-ultraviolet to violet region (299.77–424.17 nm). The spontaneous radiation for the other nine transition systems is relatively weak. 3) The $\tau_{\upsilon'J'}$ values of the (2)$2^{1st\ well}$(υ' = 0–2, +), (2)$1^{1st\ well}$(υ' = 0–2, +), and (3)0^+(υ' = 0–2, +) states gradually increase with increasing J'.

Data Availability Statement

The datasets supporting the findings of this study are available in the Science Data Bank at https://www.doi.org/10.57760/sciencedb.j00213.00233.

References

[1] McGuire B A 2022 *Astrophys. J. Suppl. S.* **259** 30

[2] Benz A O, Bruderer S, van Dishoeck E F, Stäuber P, Wampfler S F, Melchior M,

Dedes C, Wyrowski F 2010 *Astron. Astrophys.* **521** L35

[3] Godard B, Falgarone E, Gerin M, Lis D C, De Luca M, Black J H, Goicoechea J R, Cernicharo J, Neufeld D A, Menten K M, Emprechtinger M 2012 *Astron. Astrophys.* **540** A87

[4] Möller T, Schilke P, Schmiedeke A, Bergin E A, Lis D C, Sánchez-Monge Á, Schwörer A, Comito C 2021 *Astron. Astrophys.* **651** A9

[5] Müller H S P, Goicoechea J R, Cernicharo J, Agúndez M, Pety J, Cuadrado S, Gerin M, Dumas G, Chapillon E 2014 *Astron. Astrophys.* **569** L5

[6] Muller S, Müller H S P, Black J H, Gérin M, Combes F, Curran S, Falgarone E, Guélin M, Henkel C, Martín S, Menten K M, Roueff E, Aalto S, Beelen A, Wiklind T, Zwaan M A 2017 *Astron. Astrophys.* **606** A109

[7] Savage C, Apponi A J, Ziurys L M 2004 *Astrophys. J.* **608** L73

[8] Halfen D T, Ziurys L M 2015 *Astrophys. J.* **814** 119

[9] Hovde D C, Saykally R J 1987 *J. Chem. Phys.* **87** 4332

[10] Brown P R, Davies P B, Johnson S A 1986 *Chem. Phys. Lett.* **132** 582

[11] Civiš S, Blom C E, Jensen P 1989 *J. Mol. Spectrosc.* **138** 69

[12] Milan J B, Buma W J, De Lange C A 1996 *J. Chem. Phys.* **104** 521

[13] Milan J B, Buma W J, De Lange C A 1996 *J. Chem. Phys.* **105** 6688

[14] Rostas J, Horani M, Brion J, Daumont D, Malicet J 1984 *Mol. Phys.* **52** 1431

[15] Horani M, Rostas J, Roueff E 1985 *Astron. Astrophys.* **142** 346

[16] Edwards C P, Maclean C S, Sarre P J 1984 *Mol. Phys.* **52** 1453

[17] Brzozowski J, Elander N, Erman P, Lyyra M 1974 *Phys. Scr.* **10** 241

[18] Gustafsson O, Larsson M, Sigray P 1988 *Z. Physics D* **7** 373

[19] Levick A P, Sarre P J 1989 *J. Mol. Spectrosc.* **133** 227

[20] Rosmus P, Meyer W 1977 *J. Chem. Phys.* **66** 13

[21] Senekowitsch J, Werner H J, Rosmus P, Reinsch E A, Oneil S V 1985 *J. Chem. Phys.* **83** 4661

[22] Park J K, Sun H 1992 *Chem. Phys. Lett.* **194** 485

[23] González-Luque R, Merchán M, Roos B O 1992 *Mol. Phys.* **76** 201

[24] Stancil P C, Kirby K, Gu J P, Hirsch G, Buenker R J, Sannigrahi A B 2000

Astron. Astrophys. Suppl. Ser. **142** 107

[25] Shi D H, Zhang J P, Liu Y F, Sun J F, Zhu Z L 2009 *Int. J. Quantum. Chem.* **109** 1159

[26] Zanchet A, Lique F, Roncero O, Goicoechea J R, Bulut N 2019 *Astron. Astrophys.* **626** A103

[27] Zanchet A, Agúndez M, Herrero V J, Aguado A, Roncero O 2013 *Astrophys. J.* **146** 125

[28] McMillan E C, Shen G, McCann J F, McLaughlin B M, Stancil P C 2016 *J. Phys. B: At. Mol. Opt. Phys.* **49** 084001

[29] Song Y Z, Zhang Y, Gao S B, Meng Q T, Wang C K, Ballester M Y 2018 *Mol. Phys.* **116** 129

[30] Zhu Z L, Zhang A J, He D, Li W T 2021 *Phys. Chem. Chem. Phys.* **23** 4757

[31] Khadri F, Ndome H, Lahmar S, Lakhdar Z B, Hochlaf M 2006 *J. Mol. Spectrosc.* **237** 232

[32] Liu X Y, Yang C L, Wang M S, Ma X G, Liu W W 2012 *Comput. Theor. Chem.* **979** 44

[33] Xiao Z Y, Ren X Y, Liu Y, Yan B 2021 *J. Quant. Spectrosc. Ra.* **267** 107624

[34] *MOLPRO*, version 2010.1, a package of ab initio programs, Werner H J, Knowles P J, Lindh R, Manby F R, Schütz M http://www.molpro.net [2025-10-19]

[35] Li R, Dou R L, Gao T, Li Q N, Song C Q 2025 *Acta Phys. Sin.* **74** 123102

[36] Xing W, Li S Z, Sun J F, Li W T, Zhu Z L, Liu F 2022 *Acta Phys. Sin.* **71** 103101

[37] Xing W, Li S Z, Sun J F, Cao X, Zhu Z L, Li W T, Li Y Y, Bai C X 2023 *Acta Phys. Sin.* **72** 163101

[38] Xing W, Li S Z, Zhang F, Sun J F, Li W T, Zhu Z L 2024 *Acta Phys. Sin.* **73** 223101

[39] Kendall R A, Dunning Jr T H, Harrison R J 1992 *J. Chem. Phys.* **96** 6796

[40] Dunning Jr T H, Peterson K A, Wilson A K 2001 *J. Chem. Phys.* **114** 9244

[41] Oyeyemi V B, Krisiloff D B, Keith J A, Libisch F, Pavone M, Carter E A 2014 *J. Chem. Phys.* **140** 044317

[42] Dunning Jr T H 1989 *J. Chem. Phys.* **90** 1007

[43] de Jong W A, Harrison R J, Dixon D A 2001 *J. Chem. Phys.* **114** 48

[44] Woon D E, Dunning Jr T H 1993 *J. Chem. Phys.* **98** 1358

[45] Wolf A, Reiher M, Hess B A 2002 *J. Chem. Phys.* **117** 9215

[46] Peterson K A, Dunning Jr T H 2002 *J. Chem. Phys.* **117** 10548

[47] Berning A, Schweizer M, Werner H J, Knowles P J, Palmieri P 2000 *Mol. Phys.* **98** 1823

[48] Le Roy R J 2017 *J. Quant. Spectrosc. Ra.* **186** 167

[49] Sansonetti J E, Martin W C 2005 *J. Phys. Chem. Ref. Data* **34** 1559